The anomalously small 2019 Antarctic ozone hole in an assimilation of MLS observations with the GEOS Constituent Data Assimilation System

Krzysztof Wargan[1,2], Brad Weir[3,2], Gloria L Manney[4,5], Stephen Cohn[2] & Nathaniel J Livesey[6]

[1] Science Systems and Applications Inc., Lanham, Maryland, USA
[2] Global Modeling and Assimilation Office, NASA Goddard Space Flight Center, Greenbelt, Maryland, USA
[3] Universities Space Research Association, Columbia, Maryland, USA
[4]NorthWest Research Associates, Socorro, NM, USA
[5]Department of Physics, New Mexico Institute of Mining and Technology, Socorro, NM, USA
[6]Jet Propulsion Laboratory, California Institute of Technology, Pasadena, CA, USA

Corresponding author: Krzysztof Wargan (Krzysztof.Wargan-1@nasa.gov)

Key points

- The 2020 ozone hole area was about 10 million km^2 or less, compared to climatological maximum of about 23 million km^2
- The anomalously high Antarctic total ozone resulted from an unusual polar vortex size and geometry rather than from chemistry
- Even a minor sudden stratospheric warming in the Southern Hemisphere can have a big impact on polar total ozone

Abstract

A rare disturbance of the stratospheric Antarctic polar vortex in September 2019 led to a significantly higher than usual polar total ozone column. We use assimilation of ozone, HCl, and N_2O data from the Microwave Limb Sounder with the Global Earth Observing System Constituent Data Assimilation System driven by reanalysis meteorology to study the evolution of the 2019 Antarctic polar ozone. We find that the maximum 2019 ozone hole area was near 10 million km^2, and as little as 20% of that in 2018 in mid-September. However, the magnitude of vortex-averaged chemical ozone depletion was not significantly different between the two years despite earlier chlorine deactivation in 2019. The assimilation results show that most of the differences between 2018 and 2019 Antarctic ozone resulted from two factors: (1) the geometry of the 2019 vortex, with ozone-rich middle-stratospheric air masses overlying the lower portion of the vortex and leading to a significant reduction of the total column; (2) significantly reduced vortex volume. The anomalously small ozone hole of 2019 was comparable in size to the record breaking 2002 case and the mechanisms responsible were similar in the two cases. While the 2019 sudden stratospheric warming is classified as minor, its impact on ozone was very significant.

Plain language summary

A significant dynamical disturbance of the stratospheric polar vortex occurred over Antarctica in September 2019. Named sudden stratospheric warmings (SSWs), such events are relatively common in the northern hemisphere but exceedingly rare over the southern high latitudes. SSWs are known to impact polar stratospheric ozone by disturbing its chemical composition and slowing down the reactions that lead to ozone depletion. In this paper we use observations of chemical composition of the 2019 Antarctic polar vortex from NASA's satellite sensor, the Microwave Limb Sounder, combined with a Global Earth Observing System model simulation to study the chemistry and dynamics of this unusual polar winter/spring season. We show that the 2019 SSW, although not classified as "major", led to more than a 50% reduction of the ozone hole area at its peak extent, compared to other years since 2004. Furthermore, we demonstrate that most of this reduction was caused by an unusual geometry and small size of the polar vortex, while the chemistry of the 2019 ozone hole was comparable to that in the undisturbed year 2018. The 2019 event can be regarded as an example of a minor sudden stratospheric warming with a major impact.

1. Introduction

Ozone holes, defined as regions with total ozone column of 220 Dobson units (DU) or less, have formed over Antarctica every austral spring since the early 1980s (Farman et al., 1985; Komhyr et al., 1986; Stolarski et al., 1986) and constitute the most dramatic manifestation of the 20th century anthropogenic ozone destruction. They arise mainly as a result of catalytic depletion of ozone by chlorine converted from its reservoir species, HCl and $ClONO_2$, into chemically active compounds on the surfaces of Polar Stratospheric Clouds (PSCs), with an additional contribution from active bromine (Brasseur and Solomon 2005). The main source of chlorine is photodissociation of industrial chlorofluorocarbons emitted in the 20th century. Antarctic ozone depletion starts as early as late June and becomes rapid in late August and September when a significant portion of the polar vortex is exposed to sunlight that breaks ClO dimer (ClOOCl) molecules releasing atomic chlorine. The maximum and, in fact, almost complete chemical depletion occurs in the lower-stratospheric portion of the polar vortex between about 15 km and 20 km above the sea level, where temperatures are low enough for PSCs to form. The intensity of springtime polar ozone depletion depends on the amount of available chlorine as well as on the meteorological conditions in the polar stratosphere. The latter affect the temperature dependent amount of PSCs, the diabatic descent of air within the polar vortex, which resupplies ozone in the lower stratosphere (LS), permeability of the vortex edge, and the position and size of the vortex, controlling the fraction of the vortex air exposed to sunlight (WMO 2011). As stratospheric concentrations of total inorganic chlorine and bromine slowly decrease owing to the implementation of the Montreal Protocol and its amendments, the formation of ozone holes is expected to cease in the second half of the 21st century. Several recent studies found evidence of an emerging negative trend in the ozone hole sizes pointing to a gradual healing tendency of polar ozone (Solomon et al., 2016; Strahan and Douglass 2018; WMO 2018) and there is a broader effort to understand trends in ozone throughout the atmosphere (Bourassa et al., 2014, Harris et al., 2015, Ball et al., 2017, 2018, Sofieva et al., 2017, Steinbrecht et al., 2017; Wargan et al., 2018; Orbe et al., 2020; WMO 2018; SPARC/IO3C/GAW 2019).

Unlike in the Arctic, the year-to-year variability of the Antarctic ozone is small compared to the magnitude of chemical loss. Multiple studies demonstrated that, in both hemispheres, this interannual variability is primarily dynamically controlled, with more wave activity linked to higher total ozone. For example, Weber et al. (2003) showed that there is a very strong correlation between the high latitude eddy heat flux at 100 hPa and spring-to-fall ratio of high-latitude total ozone. Dynamically controlled interannual variability of Antarctic stratospheric ozone is considerably smaller than that of its Arctic counterpart, due to a significantly greater stability of the polar vortices in the Southern Hemisphere (SH). In particular, while major sudden stratospheric warmings (SSWs: Butler et al., 2017), defined as reversal events of the 60°S/N zonal mean zonal winds at 10 hPa, are common in the Northern Hemisphere (NH), only one major SSW in the SH occurred since at least the late 1950s (Naujokat and Roscoe 2005; Roscoe et al., 2005). The SH major SSW occurred in late September 2002 and was a 'split' event that led to an almost complete disintegration of the polar vortex. As a consequence, the 2002 ozone hole was significantly smaller than in the previous decade (Varotsos et al., 2002; Allen et al., 2003; Baldwin et al., 2003; Scaife et al., 2003; Sinnhuber et al., 2003; Stolarski et al. 2003; Manney et al., 2005; Newman and Nash 2005; WMO 2006).

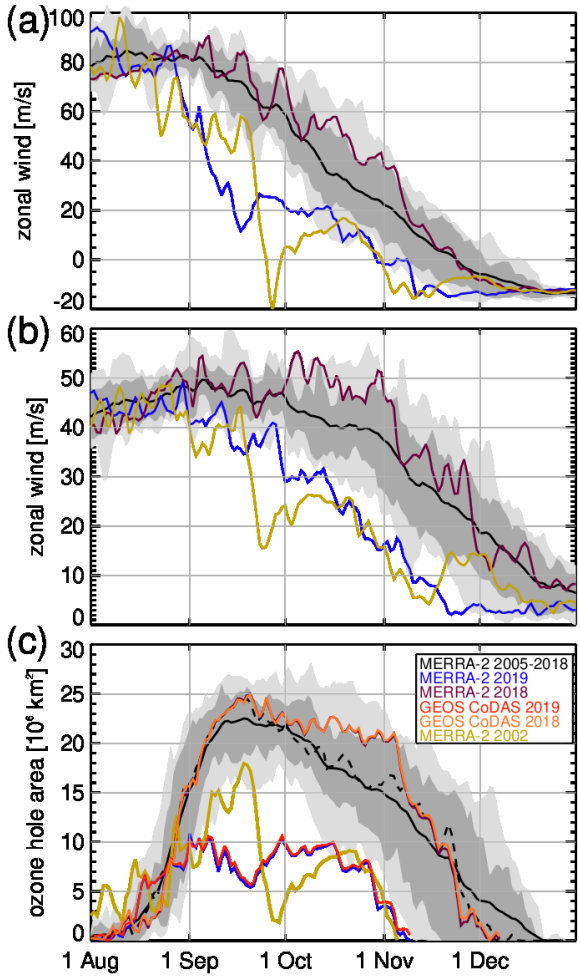

Figure 1. *The top two panels: time series of the MERRA-2 zonal mean zonal wind at 60°S in 2018 (dark magenta), 2019 (blue), and 2002 (yellow) at 10 hPa (a) and 70 hPa (b). Panel (c) shows the time series mean (solid black) and median (dashed black) ozone hole area calculated from the MERRA-2 daily total ozone between 2005 and 2018, along with the results from MERRA-2 and GEOS CoDAS for 2018 and 2019. The yellow line shows the MERRA-2 ozone hole area in 2002. In all panels the dark and light gray shading represents the 60th and 95th percentiles for the 2005–2018 period.*

In 2019, a very strong displacement of the SH polar vortex developed at the end of August (Hendon et al., 2019; Yamazaki et al., 2020). While the event did not meet the criteria of a major SSW it led to a significant weakening of the middle stratospheric zonal winds and strongly impacted polar ozone. Figure 1 shows the evolution of the 2002, 2018, and 2019 60°S zonal mean zonal wind at 10 hPa and 70 hPa, and the ozone hole area from the Modern-Era Retrospective Analysis for Research and Applications, Version 2 (MERRA-2: Gelaro et al. 2017; GMAO 2015a, 2015b) and a Global Earth Observing System (GEOS) assimilation discussed below, along with the 2005–2018 mean, 60 and 95 percentiles derived from MERRA-2. Evident is a rapid deceleration of the 10 hPa 60°S zonal wind starting in late August 2019 associated with the minor SSW. By mid-September the winds had dropped from 80 m/s to less than 20 m/s and stayed well below the average for the remainder of the austral spring season. At 70 hPa the mean zonal wind stayed below the 5th percentile threshold from September through November, indicative of the polar

vortex disturbance extending into the lower stratosphere. While there was no zonal wind reversal in 2019 the wind deceleration at 10 hPa was significant and during most of September the 2019 wind speed was at least as low or lower than in 2002. At 70 hPa the 2002 SSW was more dramatic than the 2019 SSW, with the zonal wind dropping rapidly to record low values in the second half of September. While the 2019 event is not classified as a major SSW, the synoptic conditions in 2019 were well outside the relatively tight climatological envelope, especially in the middle stratosphere. In the NH, a 10 hPa zonal mean zonal wind that is 50 m/s below the climatological mean (which is about 35 m/s in the NH in December) would be easterly and such an SSW would be classified as major. As expected from theory, the SSW led to an anomalously small ozone hole in 2019. Starting 1 September, the area of the ozone hole stayed below 10 million km^2 for the rest of the season, well below the 5^{th} percentile of the climatology. In mid-September, the 2019 ozone hole area was 5–7 million km^2, compared to the mean and median values of about 22 million km^2 and the 2018 maximum of 25 million km^2. Compared to the 2002 case, the development of the 2019 ozone hole stalled much sooner, consistent with the different timings of the two SSW events. While in 2019 the ozone hole area remained within the 5–10 million km^2 range throughout September and October, in 2002 the area dropped to near 2 million km^2 at the end of September before a partial recovery in the second half of October, after which both cases followed a very similar trajectory. In addition to the MERRA-2 results, the plot also shows the 2019 and 2018 ozone hole areas from a chemical data assimilation experiment discussed later in the paper. Here, we note that the results are almost identical between the two types of assimilation experiments.

The purpose of this study is to

- Document the evolution of the Antarctic ozone in the austral summer and spring of 2019 against the typical case of 2018
- Analyze the contributions of the polar vortex dynamics and chlorine chemistry to the unusually high total ozone values over Antarctica in 2019

Our primary data sets are obtained through data assimilation, a method of combining and propagating information from observations in space and time using the governing equations for the atmospheric state, and error estimates. A detailed theoretical description of this methodology is given in Cohn (1997). In particular, data assimilation allows generation of high-resolution and high-frequency global distributions of atmospheric constituents even from relatively sparse data by updating the prior obtained from previous assimilation steps and model integration by successive applications of Bayes' theorem as new data become available. While the dynamical fields from assimilation, and from atmospheric reanalyses in particular, have been widely used in research, the use of assimilated constituent fields is an emerging area of scientific inquiry. To date, the utility of data assimilation for scientific studies has been explored for ozone (for example, Jaeglé et al., 2017; Knowland et al., 2017, Wargan et al., 2018). The first comprehensive chemical reanalysis of the stratosphere that utilizes a full chemistry model was done at the Belgian Institute for Space Aeronomy. Named, the Belgian Assimilation System for Chemical ObsErvations (BASCOE) Reanalysis of Aura MLS, version 2 (BRAM2: Errera et al. 2019) it also assimilates MLS observations of a number of stratospheric constituents and compares well with independent observations. This study is the first one to introduce a similar stratospheric chemical assimilation system developed at NASA GMAO. We highlight some similarities and differences between our approach and BRAM2 in Section 2.

The paper is organized as follows. Section 2 describes the assimilated and independent data sets used in this study, the assimilation system, and the methodology. Section 3 evaluates the assimilation results against both the assimilated and independent observations. In Section 4 we present the results. Section 5 is devoted to a discussion of uncertainties related to model transport by assimilated winds. Section 6 summarizes the main conclusions of the study.

2. Data and methods

2.1. Assimilated observations

We assimilate observed stratospheric profiles of ozone, HCl, N_2O, water vapor, and HNO_3 from the MLS instrument onboard NASA's Aura satellite. MLS (Waters et al., 2006) measures thermal radiation in a broad spectrum of microwave bands allowing high-quality retrievals of temperature and stratospheric concentrations of a wide variety of constituents. The instrument provides a day and night near-global coverage between 82°S and 82°N. We use version 4.2 of the MLS retrievals and follow the data usage recommendations delineated in Livesey et al. (2018). Previous MLS data versions have been evaluated by Froidevaux et al. (2008a) (stratospheric ozone), Froidevaux et al. (2008b) (HCl), Lambert et al. (2007) (N_2O and water vapor), and Santee et al. (2007) (HNO_3). Table 1 summarizes the vertical ranges, resolution information and the treatment of observation errors employed in this study. Because of instrument anomalies, MLS data do not exist for three periods in 2018: 4–11 June, 21–26 June, and 10–19 July. When the data assimilation system runs with no observations for an extended period of time the results are subject to cumulative model errors. We indicate the periods of missing data in figures by hatching where appropriate. Additionally, the system assimilates total ozone column observations from the OMI instrument also onboard Aura (Levelt et al., 2006; 2018) in the same way as it is done in MERRA-2 (Wargan et al., 2017).

Table 1. Treatment of MLS observations.

Constituent	Vertical range	Vertical resolution in lower to middle stratosphere	Remarks
Ozone	216 hPa – 0.1 hPa	2.5 km – 3 km	Observation errors are calculated as in Wargan et al. (2017)
HCl	100 hPa – 0.32 hPa	3 km	Observation errors calculated as for ozone and scaled with a coefficient tuned using the approach of Desroziers et al. 2005
N_2O	68 hPa – 0.46 hPa	4 km – 6 km	Observation errors as for HCl
H_2O	215 hPa – 0.01 hPa (model top)	1.5 km – 3 km	Observation errors as for HCl
HNO_3	215 hPa – 1.5 hPa	4 km – 4.5 km	Observation errors as for HCl. HNO_3 is not assimilated in regions where model-generated PSCs are present

2.2. Data assimilation system

The data assimilation system used in this work is the GEOS Constituent Data Assimilation System (GEOS CoDAS), a generalization of the carbon monoxide (Tangborn et al., 2009), carbon dioxide (Tangborn et al., 2013; Eldering et al., 2017), and ozone (Wargan et al., 2015; 2020) assimilation systems. This work applies GEOS CoDAS to a full stratospheric chemistry model, StratChem (Kawa et al., 1995; Douglass et al., 1997; Nielsen et al., 2017). The same version of GEOS CoDAS was used by Wargan et al. (2020) where it was limited to assimilating ozone only. Here, the major advance in GEOS CoDAS is the ability to analyze a collection of constituents defined at run time and has been applied to the additional species HCl, N_2O, water vapor and HNO_3.

GEOS CoDAS uses the Gridpoint Statistical Interpolation (GSI; Wu et al., 2002, Purser et al., 2003a,b) to infer three-dimensional constituent mixing ratios on at latitude-longitude grid and terrain-following vertical levels every 6 hours. The computations for this paper were done on a 0.5×0.625-degree grid and 72 vertical levels. Retrieval error covariances were taken from the observational data product. Background error covariances are derived separately for each constituent with, at present, no correlation between different constituents. Ozone background errors are the same as that used in previous studies (Wargan et al., 2015; 2017). HCl, HNO_3, and water vapor error covariances are proportional to tracer magnitudes, thus allowing greater analysis corrections at greater tracer values. Horizontal error correlation lengths are roughly 200 km and vertical error correlation lengths are proportional to the background vertical correlation lengths. These numbers are constant throughout the atmosphere. This may seem like a simplistic assumption but, as we show in Sections 3 and 4 it does produce realistic constituent fields in agreement with observations and consistent with the underlying dynamics. N_2O background errors are treated the same as those of HCl, HNO3, and water vapor except that the error covariances are not proportional to its value. All observation error covariances were tuned using analysis diagnostics (Desroziers et al., 2005). As in Wargan et al. (2020) the wind, temperature, surface pressure and tropospheric water vapor are replayed to the MERRA-2 three-hourly averaged assimilated fields (GMAO 2015c) as described in Orbe et al. (2017). Lawrence et al. (2018) demonstrated that the reanalysis meteorology is suitable for polar processing studies.

GEOS CoDAS is similar to BRAM2 (Errera et al., 2019) in that it assimilates MLS constituent data with a system equipped with a full chemistry model but several differences exist: the use of three-dimensional variational data assimilation in GEOS CoDAS (ensemble Kalman filter in BRAM2), higher horizontal and vertical resolution, replay method of driving the meteorology (a chemistry transport model approach in BRAM2), and a smaller number of assimilated species, in addition to different chemistry models used by the two groups. A future study will present a comprehensive comparison of the two analyses.

2.3. Independent data

The Atmospheric Chemistry Experiment Fourier Transform Spectrometer (ACE-FTS: Bernath et al., 2005) measures the extinction of solar radiation between 2.2 μm and 13.3 μm at sunrise and sunset, producing about 30 profiles per day. Version 3.6 of the ACE-FTS data used in this study contains retrievals of temperature, pressure, and mixing ratio profiles of over 30 trace gases. Sheese et al. (2017) found that ACE-FTS ozone is within 5% of that measured by MLS and the Michelson Interferometer for Passive Atmospheric Sounding in the middle stratosphere. To our knowledge there are no comprehensive validation results of the recent versions of the ACE-FTS HCl. An older version (v2.2) was evaluated by Mahieu et al. (2008), who found that the mean HCl

from ACE-FTS agrees with other data sets to within 5–10%. Froidevaux et al. (2008b) calculated difference standard deviations between the ACE-FTS and MLS (Version 2.2) HCl and found them to be about 12% between 40 hPa and 10 hPa and up to 40% at 100 hPa. It should be noted that these are global comparisons. ACE-FTS data were recently used by Errera et al. (2019) for a comprehensive evaluation of the BRAM2 reanalysis of the stratosphere.

South Pole electrochemical concentration cell ozonesondes (Hassler et al., 2011) are launched on research balloons from the Amundsen-Scott South Pole station (90ºS) one to two times a week during the austral summer and spring seasons. The ozonesondes provide highly accurate measurements of ozone profiles up to about 34 km above the sea level at a resolution of 100 m. The ozonesonde data are curated by the National Oceanic and Atmospheric Administration's Earth System Laboratory (Johnson et al., 2018).

2.4. Methods

We performed several assimilation experiments using the setup described in Section 2.2. In addition to experiments assimilating all the MLS data as delineated above (ozone, HCl, HNO_3, water vapor and N_2O) between 1 June and 30 November 2018 and 2019, we used two modified system configurations. The first one uses a *passive ozone tracer* instead of assimilated ozone. The passive tracer was initialized from assimilated ozone on 29 May 2018 and 2019 and then advected by the MERRA-2 analysis winds until 30 November, with chemistry turned off. The second configuration initialized N_2O with the assimilated values also on 29 May and was run without assimilation thereafter. We use the passive ozone tracer to estimate chemical ozone depletion in Section 4, and the passive (not assimilated) N_2O to discuss model transport uncertainties in Section 5.

Of the assimilated constituents, we discuss only ozone, HCl, and N_2O. While water vapor and nitric acid are critical components of polar processing during winter and spring seasons, our goal is to examine the conditions that directly control ozone depletion within the polar vortex: the vortex size and shape and the timing of chlorine activation, here estimated from the evolution of the chlorine reservoir, HCl. We use assimilated N_2O to gain insights into the key transport processes: diabatic descent of air inside the vortex and mixing across the vortex edge. The other assimilated constituents require further evaluation that will be presented in a future publication.

To examine transport processes, we map analyzed tracer concentrations onto two types of dynamical coordinates: potential temperature (theta, vertical) and equivalent latitude (horizontal). The use of potential temperature allows one to distinguish between relatively rapid adiabatic transport that takes place on isentropic (constant theta) surfaces from slower diabatic descent inside the polar vortex. Equivalent latitude is defined as the latitude that encloses the same area as a given PV contour (Butchart and Remsberg, 1986). An air parcel maintains its equivalent latitude under reversible processes such as planetary wave driven advection. Consequently, mapping a tracer into the equivalent rather than geographical coordinate effectively removes the tracer variability associated with reversible meridional transport due to non-breaking waves, thus emphasizing those changes that result from wave-breaking driven mixing, chemistry, and diabatic processes. We define the polar vortex edge using a potential temperature dependent profile of PV scaled in "vorticity units" (e.g., Dunkerton and Delisi, 1986; implementation as in Manney, et al., 1994; referred to hereinafter as sPV), with the values at each level defined by examination of winter

mean sPV gradients as a function of equivalent latitude, as described by Lawrence et al. (2018). As discussed by Lawrence and Manney (2019), a single value determined by examination of season-long climatology has several advantages over criteria determined on a daily basis (such as that developed by Nash et al, 1996), especially early and late in the season and other times when the vortex is disturbed (which can result in spikes or discontinuities in the vortex edge definition), and for interannual comparisons such as done in this paper.

Formation of nitric acid trihydrate (NAT) PSCs occurs when the air temperature falls below a threshold value, T_{NAT}. In our diagnostics (Figure 12) we use pressure dependent T_{NAT} values calculated in Lawrence et al. (2018) (their Table A2) and interpolated linearly in potential temperature.

3. Performance of GEOS CoDAS

In this section we compare the analysis ozone, HCl, and N_2O from the 2019 GEOS CoDAS experiment with observations from MLS and ACE-FTS. Comparisons of the analysis to MLS provide a measure of the agreement between the analysis fields and the assimilated data. In a well-tuned system, we expect the agreement to be comparable in magnitude to the estimated observation uncertainties. Comparisons with ACE-FTS serve as independent evaluation of the analysis. While the coverage of MLS in the region of interest (90°S–30°S) is nearly complete, the number of ACE-FTS observations is limited due to the nature of the solar occultation measurement technique as well as strong seasonal variations of the observed latitudes (Bernath 2017, their Figure 6). We performed the ACE-FTS comparisons for the period between 1 June and 30 September 2019 as there were no data in the polar region in October and November. For MLS, the period of comparison is 1 July to 30 November 2019. We did the ozone and HCl comparisons on 6 selected pressure levels: 100 hPa, 70 hPa, 50 hPa, 30 hPa, 20 hPa, and 10 hPa. For N_2O, we used 50 hPa and 70 hPa as the lowest levels for comparisons with MLS and ACE-FTS, respectively. The analysis data were subsampled at the geographical locations of the observations.

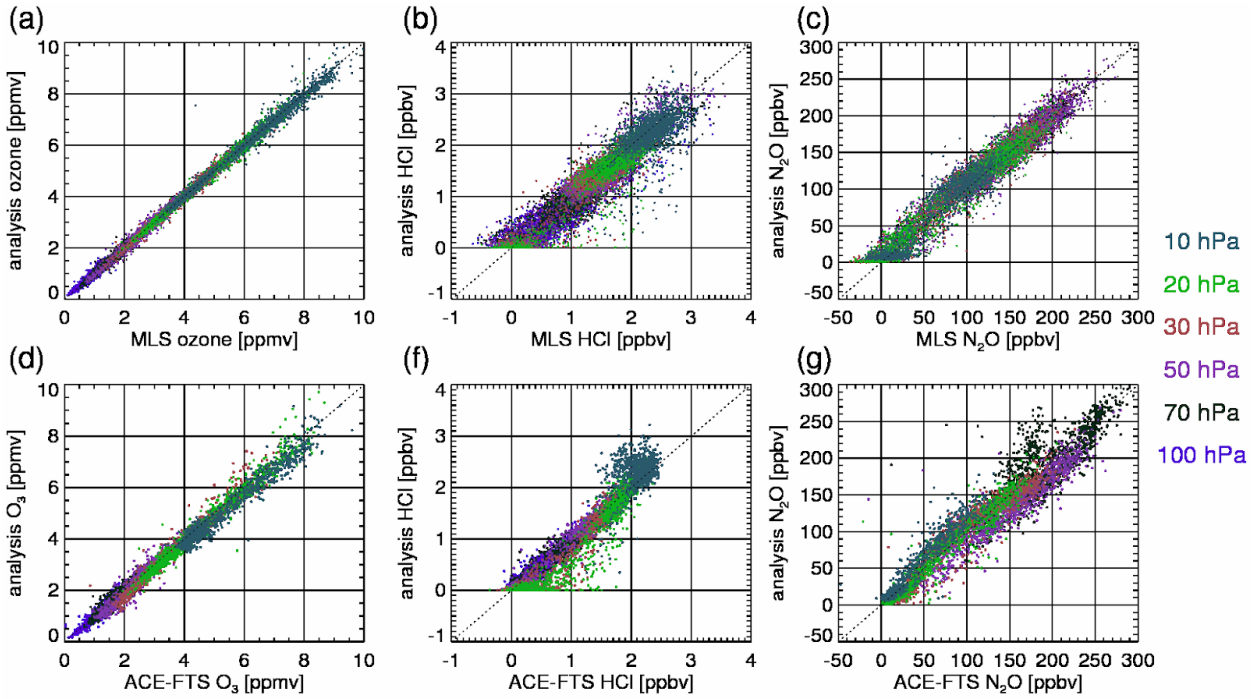

Figure 2. *Comparisons of GEOS CoDAS ozone (a and d), HCl (b and f), and N_2O (c and g) with the assimilated MLS (a–c) and ACE-FTS (d–g) data between 90°S and 30°S. The analysis fields are subsampled at the observation locations and the observations are interpolated to selected analysis pressure levels between 100 hPa and 10 hPa (50 hPa to 10 hPa for MLS N_2O, and 70 hPa to 10 hPa for ACE-FTS N_2O). MLS data between 1 July and 30 November 2019 and ACE-FTS observations between 1 June and 30 September are used. All available ACE-FTS data from that period are used, while 2,000 randomly selected MLS data per theta level are used.*

Figure 2 shows the results in a form of scatterplots. For MLS, due to a very large number of data points we show 2,000 randomly selected data points for each level, but we calculate the statistics (see below) from the full data set. Tables 2 and 3 show the corresponding statistics for MLS and ACE-FTS, respectively: the mean difference and difference standard deviations relative to the satellite average, and correlations.

As seen in Figure 2a and c, and in Tables 2 and 3 the analysis ozone is in excellent agreement with both satellite data sets. As expected, the agreement with the assimilated MLS observations is very good, with virtually no bias and difference standard deviations within 5% at pressures greater than or equal to 50 hPa and within 10% at higher pressures. There is a small negative bias with respect to ACE-FTS. The difference standard deviations with ACE-FTS are within 10% at pressures less than 100 hPa, and ~12% at 100 hPa. The analysis-satellite correlations are all 0.94 and higher, often above 0.99. As expected, the differences between the analysis ozone and MLS are comparable with the MLS uncertainties (Livesey et al. 2018).

Comparisons between the analysis and satellite HCl produce larger differences. The mean differences between the analysis and MLS HCl range between -4.5% and -16% (at 100 hPa), within the reported accuracy estimates for MLS. The difference standard deviations with MLS and ACE-FTS at the lowest levels (highest pressures) are quantitatively close to those in Errera et al. (2019)

for the BRAM2 reanalysis (see their Table 2) and close to the precision estimates form MLS HCl. At pressures smaller than 50 hPa the difference standard deviations are below 20% for MLS and between 14% and 24% for ACE-FTS. This is higher than the BRAM2 results at 640 K (above the layer of maximum ozone depletion). Nonetheless, the HCl variability is well represented. The correlations between the analysis and MLS HCl are between 0.64 and 0.94. For the ACE-FTS comparisons all the correlations between 100 hPa and 20 hPa are greater than 0.9. Interestingly, the correlations with ACE-FTS HCl are slightly higher than with MLS, although the difference is not large. We note, however, that the data sampling and temporal coverage differ between the two.

The mean differences between the analysis and MLS N_2O are between 1.64% and 6.55%, within or close to the MLS accuracy estimates. The difference standard deviations are between 10% and 22% with lower values at higher pressures. These values are slightly larger than the reported precision estimates. The analysis–MLS correlations are 0.95 and higher at all levels. The average differences between the analysis and ACE-FTS N_2O are negative between 70 hPa and 20 hPa, and range between 3% and 12%. The difference standard deviations are within 20% in that pressure range, comparable to the results reported by Errera et al. (2019) for BRAM2 in the Antarctic region. Larger discrepancies are seen at 10 hPa with the average difference close to 30%. A positive bias at 10 hPa is, in part, an expected result of a constraint forcing the analysis tracer concentrations to be non-negative, as required by the chemistry model, while many MLS N_2O observations show strongly negative values in the middle stratosphere. Livesey et al. (2018) noted that ignoring the negatives leads to an overestimation of temporal and spatial averages. We currently have no solution to this issue. However, the 10 hPa pressure level lies above the main region of interest of this study.

We provide further comparisons between the analysis and MLS data in Figure 5 discussed in Section 4.

Table 2. Mean difference (analysis minus observations), difference standard deviations and correlations between MLS ozone, HCl, and N_2O observations and collocated analysis at selected pressure levels. The mean difference and standard deviations are given relative to the mean MLS at each level. 90°S–30°S data between 1 July and 30 November 2019 are used.

	Ozone			**HCl**			**N_2O**		
Pressure [hPa]	**Mean difference [%]**	**Difference standard deviation [%]**	**R**	**Mean difference [%]**	**Difference standard deviation [%]**	**R**	**Mean difference [%]**	**Difference standard deviation [%]**	**R**
100	0.45	9.60	0.97	-15.41	43.47	0.88	-	-	-
70	-0.08	6.11	0.99	-8.90	28.76	0.92	-	-	-
50	0.81	4.51	0.99	-4.12	21.39	0.94	1.64	10.03	0.96
30	0.15	2.75	0.99	-4.89	18.36	0.93	3.98	11.52	0.97
20	-0.11	2.82	0.99	-6.73	16.31	0.94	4.10	14.13	0.97
10	-0.46	3.20	0.99	-4.44	13.60	0.64	6.55	21.68	0.95

Table 3. Mean difference (analysis minus observations), difference standard deviations and correlations between ACE-FTS ozone, HCl, and N_2O observations and collocated analysis at selected pressure levels. The Mean difference and standard deviations are given relative to the mean ACE-FTS at each level. 90°S–30°S data between 1 June and 30 September 2019 are used.

	Ozone			HCl			N_2O		
Pressure [hPa]	**Mean difference [%]**	**Difference standard deviation [%]**	**R**	**Mean difference [%]**	**Difference standard deviation [%]**	**R**	**Mean difference [%]**	**Difference standard deviation [%]**	**R**
100	-3.54	12.34	0.94	10.11	34.08	0.93	-	-	-
70	0.04	9.22	0.95	-3.37	23.54	0.97	-1.48	16.37	0.76
50	-2.34	8.05	0.96	-2.99	18.71	0.98	-12.11	12.8	0.92
30	-2.64	6.55	0.98	-12.51	23.27	0.96	-2.48	15.87	0.96
20	-2.36	6.23	0.98	-17.12	23.94	0.93	-3.87	19.39	0.97
10	-4.44	5.31	0.98	8.14	13.85	0.53	27.93	35.52	0.97

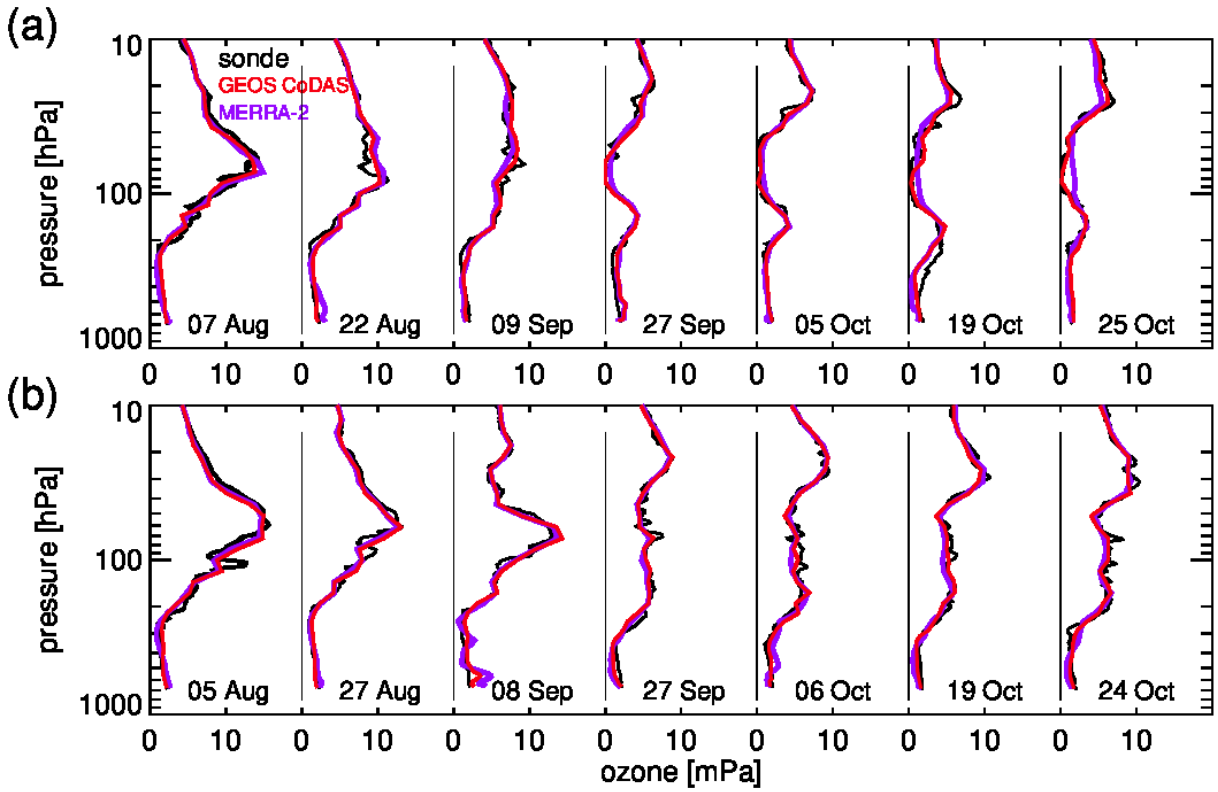

Figure 3. *South Pole ozonesonde ozone partial pressure (black), MERRA-2 (purple) and GEOS CoDAS (red) profiles at seven selected dates during the austral winter and spring in 2018 (a) and 2019 (b).*

Figure 3 shows seven selected ozone partial pressure profiles from the South Pole ozone sondes in 2018 and 2019 between early August and late October, along with ozone from MERRA-2 and GEOS CoDAS. In 2018, the ozone partial pressures between 100 hPa and 40 hPa decreased to almost zero starting in late September. This is a typical evolution of the South Pole ozone in recent decades (Bell et al., 1999, their Figure 14). By contrast, the 2019 values in that layer remain at 5 mPa or higher. The 8 September profile exhibits a pronounced maximum of about 12 mPa at 70 hPa that was absent in 2018. In the following weeks, the deep layer between 200 hPa and 30 hPa

shows relatively very high values of at least 5 mPa. In both years there is an excellent agreement between the GEOS CoDAS analysis and the ozonesondes. MERRA-2 follows the ozonesondes closely with the exception of a slight overestimations between 100 hPa and 50 hPa on 19 and 25 October 2018, which indicate an advantage in using a full chemistry model to represent Antarctic ozone loss away from observations (recall that there are no MLS data south of 82°S).

The results shown above establish the uncertainties of the analysis ozone, HCl, and N_2O. These uncertainties are the smallest for ozone, which is of main interest for this study. The following section examines the evolution of these tracers and provides process-based comparisons between the GEOS CoDAS analysis MLS data in a spatial and temporal context.

4. Evolution of the analyzed polar vortex ozone: dynamics, transport, and chemistry

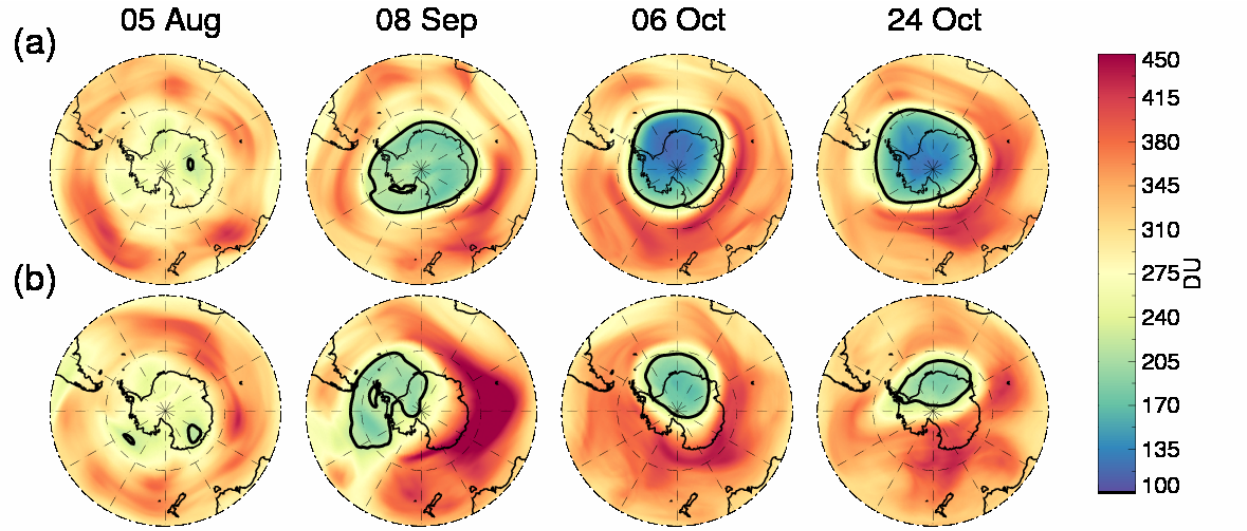

Figure 4. *Daily mean total ozone from GEOS CoDAS on 5 August, 8 September, 6 October, and 24 October 2018 (a) and 2019 (b). The black contours indicate 220 Dobson units. Plotted are latitudes between 30°S and 90°S.*

Figure 4 compares the evolution of the GEOS CoDAS total ozone in 2018 and 2019. The dates are close to those shown in Figure 3 for the South Pole ozonesondes. In early August, before the ozone hole had formed and before the 2019 vortex and temperature morphology departed substantially from climatology, the geographical distribution of total ozone was similar in both years. The situation was quite different in September and October: while in 2018 the ozone hole covered almost all of Antarctica, in 2019 its area was less than 50% of that in the preceding year, irregular in shape and shifted off the South Pole (the pole was inside the ozone hole but near its edge on 6 October), consistent with the ozonesonde soundings shown in Figure 3. In addition, the total ozone values within the ozone hole in October were larger in 2019 than in 2018. The area-averaged ozone column within the 220 DU contour was 158.4 DU on 6 October 2018 and 165.4 DU on 24 October 2018. The corresponding numbers for 2019 are 190.1 DU and 200.3 DU, respectively.

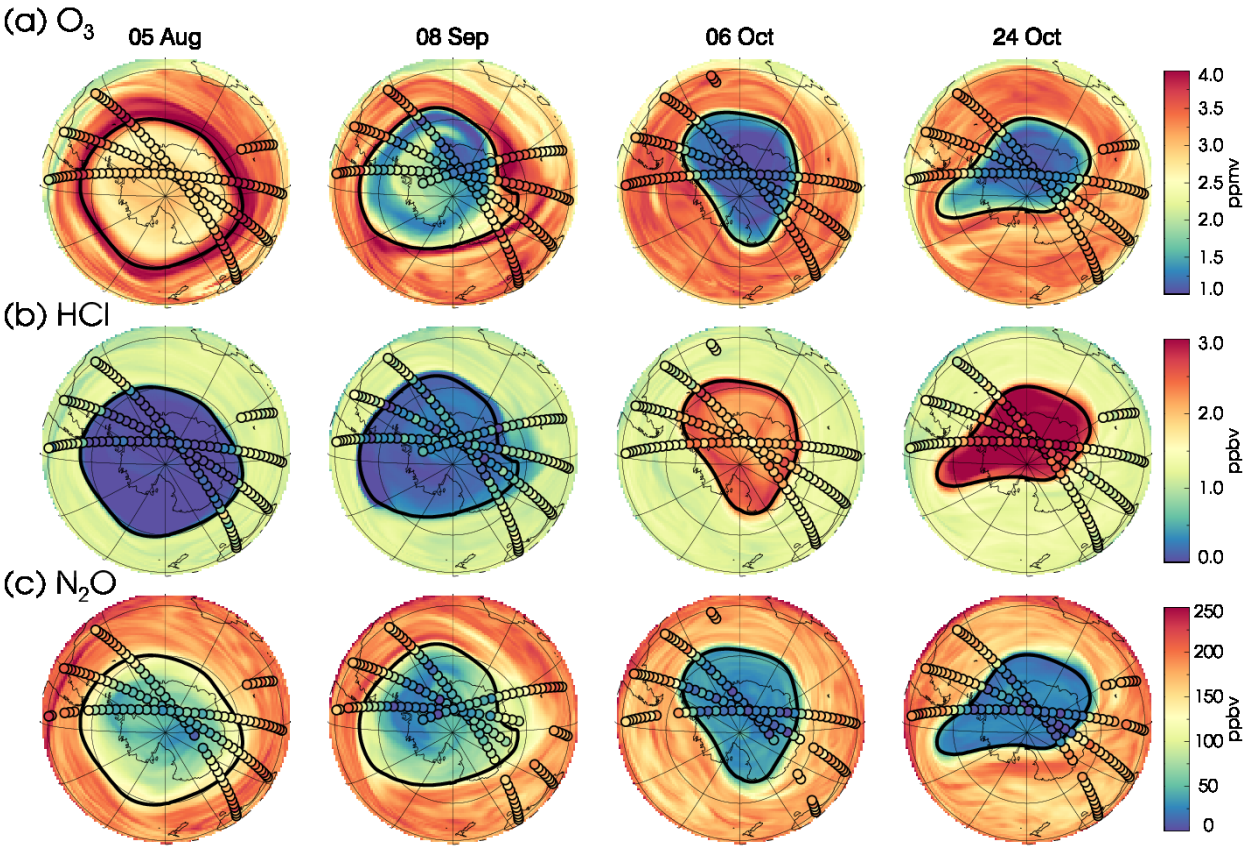

Figure 5. *Maps of analysis ozone (a), HCl (b), and N_2O (c) on the 520-K isentropic surface on 5 August, 8 September, 6 and 24 October 2019. The circles show locations and values of the assimilated MLS observations. The black contours mark the edge of the polar vortex.*

Figure 5 shows 12 UTC ozone, HCl, and N_2O on the 520-K isentropic surface (inside the polar vortex, that correspond to altitudes between 20 km and 22 km above the mean sea level) on the same four dates in 2019. It also plots the MLS measurements of these constituents within ±3 hours of the analyses. As expected from chemical depletion, a decline of the vortex ozone is evident between 5 August and 6 October. It is also clear that the polar vortex at this isentropic level was disturbed and decentered in October compared to early August. On 8 September the vortex was not yet much deformed, but it had already shifted off the pole towards the eastern South Pacific. Hydrogen chloride was almost completely depleted within the vortex on 5 August, consistent with full chlorine activation. On 8 September HCl exhibited slightly larger mixing ratios and some evidence of dispersal through the vortex edge, indicated by depressed values between 60°E and 120°E and coincident with an irregularity of the vortex edge, indicative of a distortion of the PV field at 520 K. Evidence of some dispersal of the vortex material is also seen in the ozone field (Figure 5a) in the form of a local displacement of the high ozone "collar" from the vortex edge corroborated by the MLS data. By 6 and 24 October the HCl mixing ratios inside the vortex had increased from near-zero values to 2 ppbv – 2.5 ppbv and to over 3 ppbv, respectively, indicative of chlorine deactivation (see our discussion of Figure 14 below). The polar vortex N_2O exhibited a gradual decrease, starting with depressed values in the vortex core in August and September and reaching uniformly low mixing ratios in October. This was associated with a sharpening of the

N_2O gradient across the edge as the midlatitude values remained unchanged. This slow decrease is consistent with diabatic descent of the vortex air typical for both Antarctic and Arctic winters that leads to a partial replenishment of chemically depleted lower-stratospheric ozone by ozone-rich air from higher altitudes. A signature of the dispersal seen in HCl and ozone on 8 September is also present in N_2O.

The analysis ozone and N_2O in Figure 5 are in excellent agreement with the MLS data that were assimilated. For HCl, the MLS observations show considerably more variability than the analysis does. This is especially evident, but not limited to, the interior of the polar vortex. A detailed analysis (not shown) reveals that the HCl data from MLS exhibit a considerably flatter power spectrum than that derived from ozone measurements, indicative of more variability at small spatial scales. As those variabilities are controlled primarily by transport, different power spectra for different tracers likely reflect noise in the HCl data. This assertion is consistent with larger relative uncertainties in the MLS HCl compared to ozone (Livesey et al., 2018). As the assimilation algorithm takes these uncertainties into account, the HCl data are given proportionally less weight than the ozone observations. As a result, the analysis tracer spectra, unlike the observed ones, are very similar between ozone and HCl. For an animated version of Figure 5 see Movie S1. The animation shows the three species and water vapor at four isentropic levels between 520 K and 800 K.

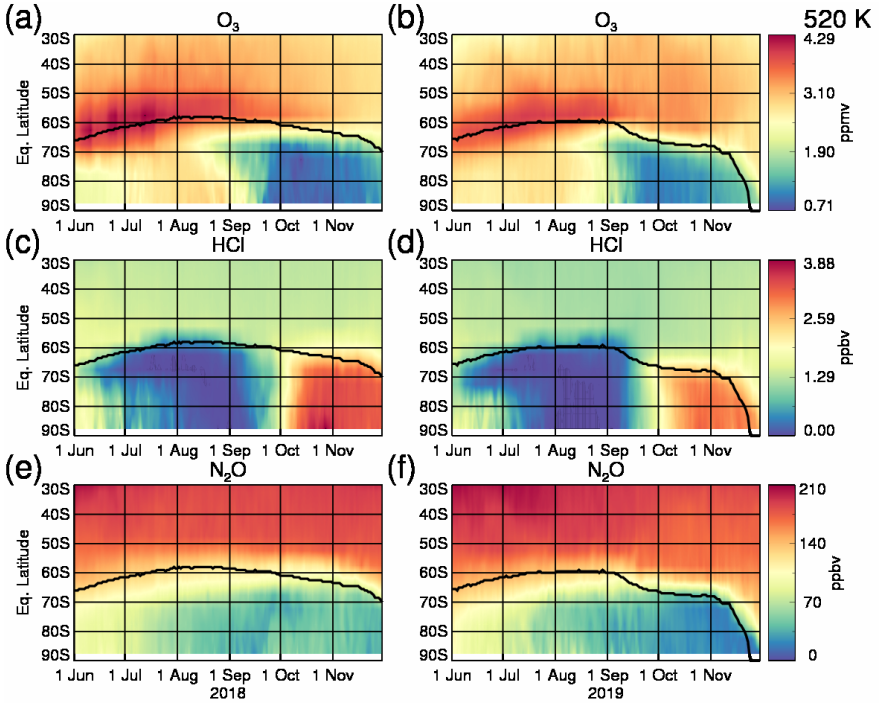

Figure 6. *Assimilated constituent mixing ratios on the 520-K isentrope as functions of time and equivalent latitude for 2018 (a, c, and e) and 2019 (b, d, and f). Shown are ozone (a and b), HCl (c and d), and N_2O (e and f). The black lines mark the edge of the polar vortex.*

Figure 6 illustrates the evolution of ozone, HCl, and N_2O on the 520-K isentropic surface as a function of equivalent latitude in 2018 and 2019. The vortex ozone between equivalent latitudes 90°S and 70°S (Figure 6a and b) in both years exhibits mixing ratios between 2.3 ppmv and 2.9

ppmv until mid-August. There is a clear signature of rapid chemical depletion starting around 15 August, first near 70°S equivalent latitude and, by 1 September, throughout the vortex. The onset of ozone depletion in the vortex core occurred about two weeks sooner in 2019 than in 2018. Both years featured a pronounced ozone collar with mixing ratios up to 3.9 ppmv around the polar vortex edge. In 2018 the vortex reached its maximum extent (58°S) in August. That was followed by a gradual shrinking to 70°S at the end of November. In 2019, the maximum vortex extent was 60°S in August. The SSW resulted in a rapid decrease by mid-September. The polar vortex had disintegrated by the end of November 2019 (one to two months earlier than typically seen in the Antarctic lower stratosphere, e.g., Manney et al. 2005). Hydrogen chloride (Figure 6c and d) underwent a fast conversion into active chlorine, as indicated by its rapid depletion inside the polar vortex in both years. Slightly elevated concentrations of HCl were seen in the vortex core until July. Rapid chlorine deactivation, indicated by the increase in the HCl concentrations, occurred at this isentropic level in late September 2018 and mid-September in 2019. The polar vortex N_2O concentrations (Figure 6e and f) exhibited a gradual decrease throughout the austral summer and spring in both years, consistent with diabatic descent of N_2O-poor mid- and upper-stratospheric air. As lower-stratospheric N_2O is chemically inactive on the timescales of interest, it serves as an excellent transport tracer. There is no evidence of significant irreversible isentropic mixing of air at the 520-K potential temperature level until late November 2019 during the final warming.

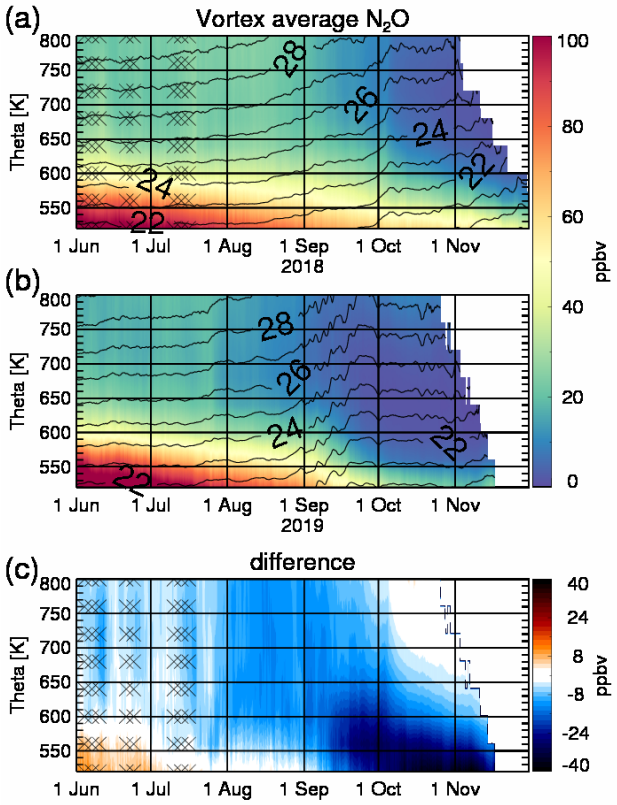

Figure 7. *N_2O mixing ratio averaged within the polar vortex as a function of time and potential temperature for 2018 (a), 2019 (b), and the difference of the two (c). The contours in (a) and (b) represent the vortex-averaged geopotential height in kilometers. The dashed contour in (c) represents zero difference. The periods in 2018 for which MLS data do not exist are indicated by hatching.*

The polar vortex ozone budget is determined by chemical depletion and dynamical resupply, mainly from diabatic descent of ozone-rich upper air and, to a much lesser extent, from mixing across the vortex edge (Manney et al., 1995a; Manney et al., 2015; Livesey et al., 2015; Strahan et al., 2016). Figure 7 shows the vortex average mixing ratio of assimilated N_2O as a function of time and potential temperature in 2018 and 2019 and the difference of the two. The plots in this figure and in Figures 8, 9, 12, and 13 also show the average vortex geopotential height contours. Unlike our other figures, this one is cut off at the 520-K isentropic level in order to show only those levels at which N_2O is assimilated (pressures greater than or equal to 68 hPa). The minor SSW resulted in a significant downward shift of the isentropes in 2019 compared to 2018. By late October the isentropic surfaces above 400 K were located about 1 km lower in 2019 than in the previous year. The gradual decline in N_2O concentrations seen in Figure 7 in both years, especially at the lower levels, is a signature of diabatic descent. A comparison of Figure 7 with a similar time series of N_2O derived directly from MLS observations (see, for example Santee et al., 2008) reveals some important differences. The analysis N_2O does not exhibit a significant signature of descent above 650 K between June and September in both 2018 and 2019, compared to, for example, Santee et al. (2008), their Figure 11. This is likely due to the analysis not reflecting the negative N_2O mixing ratios in the MLS data as well as the fact that the N_2O mixing ratios at those levels are often consistent with zero within the observation uncertainties. As a result, the vertical gradient is not accurately reproduced by the assimilation (or, indeed, MLS N_2O observations) above approximately 650 K. Consequently, the analysis N_2O is not a good indicator of mean diabatic transport in the middle-stratospheric polar vortex. However, we note that these levels lie above the layer of maximum ozone depletion. Figure 7c shows a broad descending pattern of negative differences between 2019 and 2018 N_2O starting in mid-September below 600 K, indicative of a stronger diabatic descent in 2019. This is consistent with increased radiative cooling following the SSW-induced temperature increase. This rapid descent is evident in Figure 7b between early September and late October and extends down to at least the 520-K isentropic level.

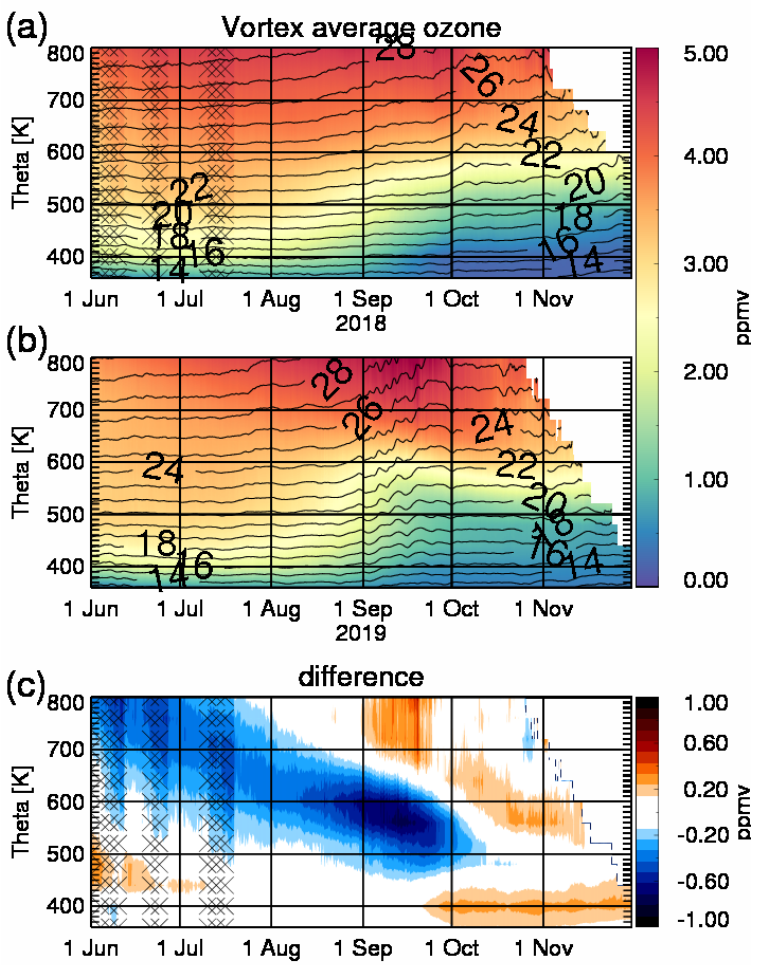

Figure 8. *Ozone mixing ratio averaged within the polar vortex as a function of time and potential temperature for 2018 (a), 2019 (b), and the difference of the two (c). The contours in (a) and (b) represent the vortex-averaged geopotential height in kilometers. The times and levels where the equivalent latitude of the vortex edge is south of 87°S (the vortex area of less than 0.001 of the earth's surface) are shown in white. The periods in 2018 for which MLS data do not exist are indicated by hatching.*

Figure 8 plots the average polar vortex ozone mixing ratios in 2018 and 2019 as functions of time and potential temperature. The values between 400 K and about 600 K rapidly decreased between mid-August and mid-September in both years. The vertical pattern of this decrease is similar to that reported by Santee et al. (2008) for the 2005 Antarctic winter (their Figure 11). Figure 8c shows the difference between the 2019 and 2018 average vortex ozone mixing ratios relative to the 2018 values. These differences result from different chemistry as well as the different rate of ozone resupply through diabatic descent. There was a descending pattern of negative (the 2019 ozone is lower) differences from June to September, culminating in an early September minimum located between 550 K and 600 K. This pattern reflects lower average ozone in the middle and upper portion of the polar vortex in 2019, brought downward by slow diabatic descent, and a larger vertical extent of chemical depletion in 2019 as discussed below (Figure 13; see also Figure S1). The vortex average ozone in 2019 was very close to the 2018 values in October and November.

The largest differences of only up to 0.3 ppmv, centered at 400 K, were small compared to about 2.5 ppmv overall decline in ozone between June and October. Until the end of September, the 2019 ozone in the lower portion of the vortex was not larger than it was in 2018. This may seem inconsistent with the results seen in Figure 1, showing 2019 ozone hole areas rapidly diverging from the 2018 values as early as in late August. The reasons for this apparent discrepancy are a substantial difference in the polar vortex size between the two winters, evident in Figure 9 and in the vertical alignment of the vortex (Figure 10). We will now discuss these two factors in detail.

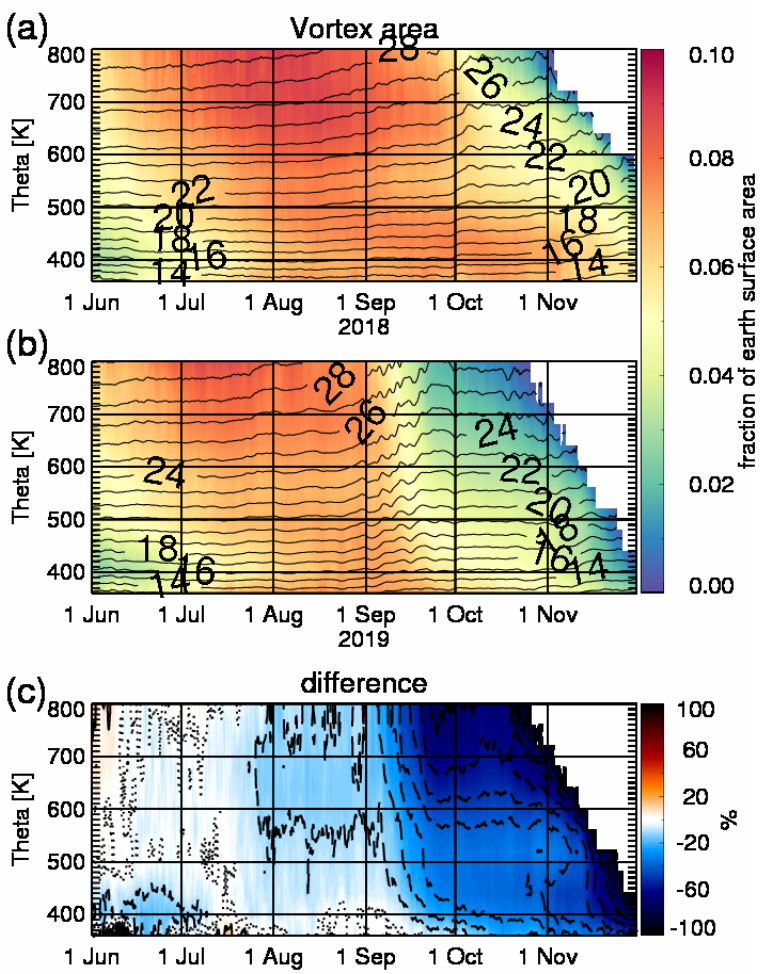

Figure 9. *Polar vortex area as a function of time and potential temperature for 2018 (a), 2019 (b), and the difference of the two, relative to the 2018 average (c). The areas are shown as fractions of the Earth's surface area. The contours in (a) and (b) represent the vortex-averaged geopotential height in kilometers. The contours in (c) are spaced by 10%, negative relative differences are shown as dashed lines. The times and levels where the equivalent latitude of the vortex edge is south of 87°S (the vortex area of less than 0.001 of the earth's surface) are shown in white.*

The 2019 areas on the isentropic surfaces between 360 K and 800 K (Figure 9) were within 10% of those in 2018 until the end of July. In August the 2019 areas above 550 K were 10%–20% smaller than in 2018. Following the onset of the SSW at the August-September boundary, the 2019 vortex areas decreased rapidly. By mid-September, the areas between 600 K and 800 K reached

about 3% of the Earth's surface area in late September, about one half of the 2018 values. Since at those levels ozone mixing ratios are much higher outside the polar vortex than inside of it, it is reasonable to expect that the size of the ozone hole (defined through a vertical integral of the mixing ratio) is in part controlled by the spatial extent of the vortex. We explore this in Figure 10, similar to a plot in Hoppel et al. (2003) for the anomalous 2002 Antarctic ozone hole.

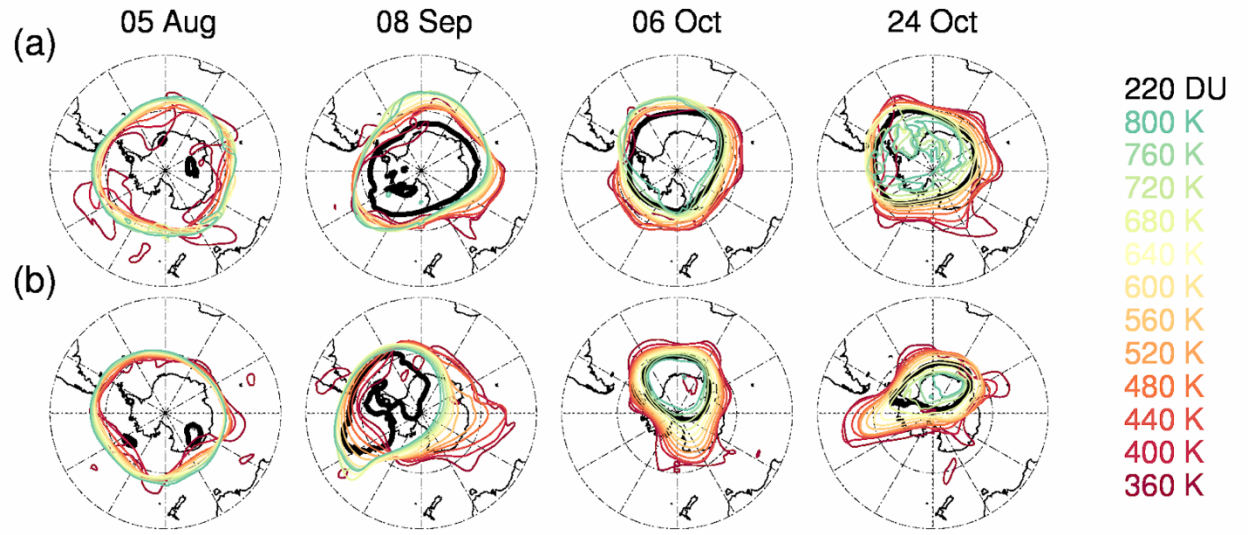

Figure 10. *Positions of the polar vortex edges on the isentropic surfaces between 360 K and 800 K and the edge of the ozone hole on 5 August, 8 September, 6 and 24 October of 2018 (a) and 2019 (b). Plotted are latitudes between 30°S and 90°S.*

The plots show the 2018 and 2019 polar vortex edges at 12 isentropic surfaces between 360 K and 800 K in 40 K increments, along with the edge of the ozone hole (220 DU) on 5 August, 8 September, and 6 and 24 October. On 5 August, the vortex extended over the entire Antarctic continent, it was nearly circular and slightly widening with height. While an ozone hole had not yet formed, two miniholes (Newman et al., 1988; Hood et al., 2001; Iwao and Hirooka 2006) were present, nested in dents of the 360-K vortex edge associated with anticyclonic anomalies in the upper troposphere - lower stratosphere. More of these dynamically driven low ozone patches are seen in an animated version of Figure 10 (Movies S2 and S3). The situation on 8 September was dramatically different. The 2019 polar vortex exhibited a westward tilt, with the base (360 K – 520 K) wider and more irregular than the middle stratospheric layer (560 K – 800 K) that was displaced toward South America (the vortex was shaped like a tilted cone). The ozone hole edge was highly irregular and positioned underneath the middle-to-upper portion of the vortex (600 K and above). The evolution of the polar vortex from that point on involved shrinking in size and further tilting (see Movie S2). Crucially, the ozone hole boundary tended to be aligned with the intersection of the vortex edges up to at least 760 K, rather than with the lower portion of the vortex where most of the ozone loss occurs. This was also the case in the undisturbed 2018 case (Figure 10a).

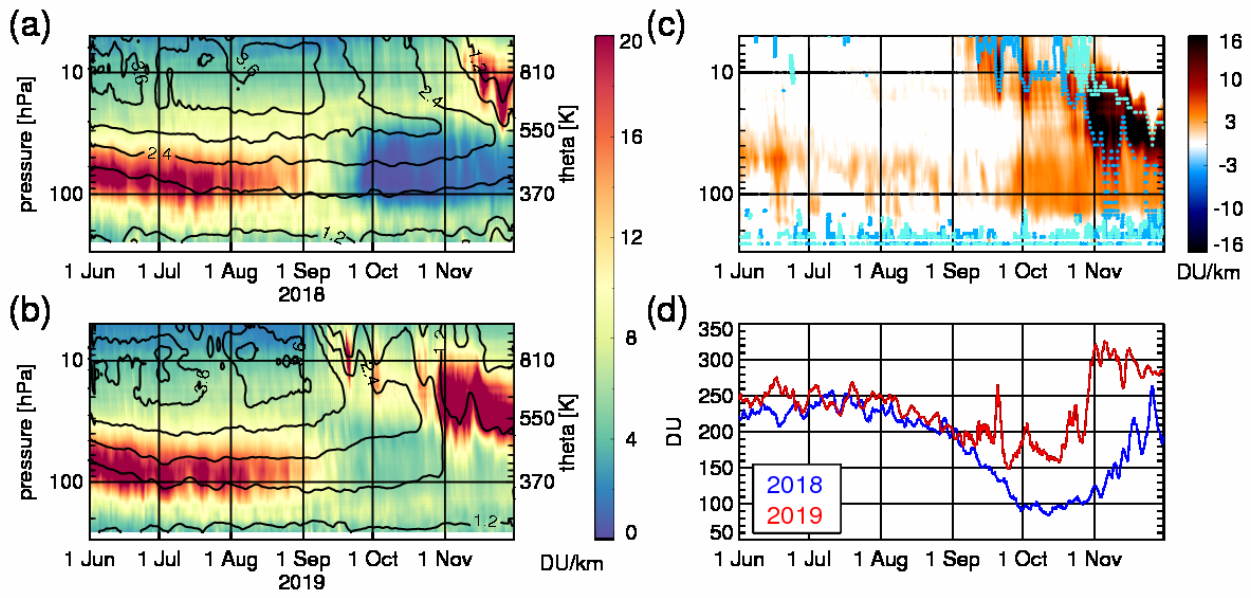

Figure 11. *(a and b) 2018 and 2019 time series of 90°S–85°S ozone profiles in DU per km as functions calculated on potential temperature levels and shown as functions of the average pressure between 250 hPa and 5 hPa. The contours show the corresponding sPV time series. (c) the 2019-2018 ozone difference calculated on potential temperature levels; the y-axis shows the corresponding average 2019 pressures. The light blue and cyan dots mark the times and levels where the edge of the polar vortex passes over the south pole in 2019, and 2018, respectively. (d) 90°S–85°S ozone vertically integrated between 300 K and 1200 K in 2018 (blue) and 2019 (red).*

These results indicate significant contributions of the entire 400 K – 800 K ozone profile to the integrated column abundances: a vortex tilt results in layers of relatively high mid-stratospheric midlatitudinal ozone concentrations sliding over the chemically depleted LS region, raising the total column values above the 220 DU threshold. This is similar to the effect that the polar vortex geometry had on total ozone during the 2002 SSW (e.g., WMO 2006). We illustrate the role of the vortex geometry in Figure 11, which shows the 2018 and 2019 evolution of the ozone profile over the south pole (the 90°S–85°S average) along with the difference between the two years (Figure 11c) and the vertical integrals between 300 K and 1200 K (Figure 11d). The profiles are shown in Dobson units per kilometer to help the reader estimate the contributions of ozone in different layers. Until the end of August there was very little difference between the 2018 and 2019 profiles and between the integrated columns, but the differences grew rapidly in September. It is clear from Figure 11c that the September differences were largely due to increased ozone at 800 K and above (pressures 20 hPa and less) and were associated with a passage of the vortex edge over the South Pole, marked by a blue dotted line in Figure 11c. This is very similar to the 2002 ozone hole evolution following the vortex split event (Kondragunta et al., 2005). The very large differences between the two years in October and November resulted from higher 2019 ozone throughout the vortex at that time: the absence of strong depletion between 360 K and 550 K, and enhanced values aloft. The latter were, again, linked to the position of that portion of the 2019 vortex. In particular, we note the very large differences between 550 K and 800 K (30 hPa – 10 hPa) in November, when the pole was outside the polar vortex in 2019 but inside of it in 2018.

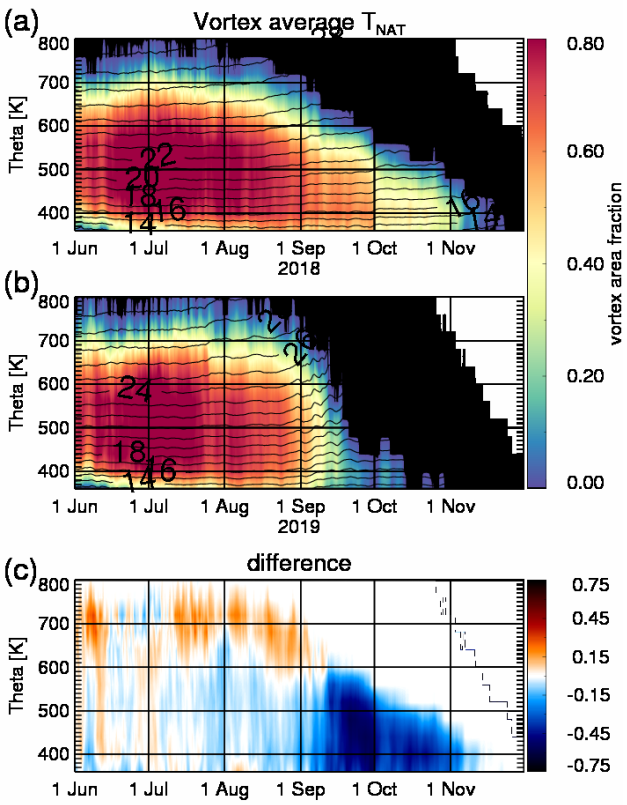

Figure 12. *Fraction of the polar vortex area with temperatures below T_{NAT} as a function of time and potential temperature for 2018 (a), 2019 (b), and the difference of the two (c). The contours in (a) and (b) represent the vortex-averaged geopotential height. The times and levels where the equivalent latitude of the vortex edge is south of 87°S (the vortex area of less than 0.001 of the earth's surface) are shown in white.*

We now turn to the factors that directly control the ozone chemistry: the vortex temperature and its relationship with chlorine activation. Figure 12 shows the fraction of the polar vortex with temperatures less than or equal T_{NAT} as a function of potential temperature and time in 2018 and 2019, and their difference. In June and July there was a large potential for PSC formation between 360 K and 700 K in both years. Sufficiently low temperatures extended over up to 80% of the polar vortex area. In 2019, these low temperatures persisted in the entire layer throughout August, whereas in 2018 the vortex fraction below T_{NAT} began to decrease between 600 K and 700 K and continued to gradually decrease until the beginning of November. In contrast, in 2019 the T_{NAT} area declined sharply to nearly zero above 500 K over the course of about three weeks, starting at the beginning of September, coincident with the SSW. The difference plot (Figure 12c) makes evident a sharp contrast between the 2019 and 2018 cases: while during August the T_{NAT} area differences were within 10% of the vortex area (larger in 2019 above 600 K and slightly smaller below that level), in September, the differences reached 50% within the first two weeks.

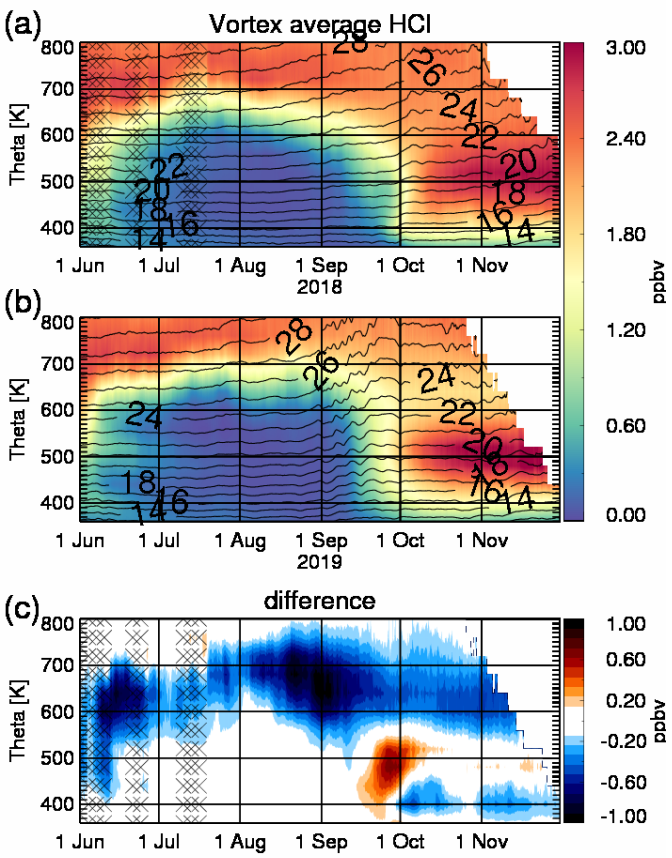

688
689 **Figure 13.** *HCl mixing ratio averaged within the polar vortex as a function of time and potential*
690 *temperature for 2018 (a), 2019 (b), and the difference of the two (c). The contours in (a) and (b)*
691 *represent the vortex-averaged geopotential height. The times and levels where the equivalent*
692 *latitude of the vortex edge is south of 87°S (the vortex area of less than 0.001 of the earth's surface)*
693 *are shown in white. The periods in 2018 for which MLS data do not exist are indicated by*
694 *hatching.*
695
696 This evolution of the lowest vortex temperatures is consistent with the behavior of the average
697 vortex mixing ratios of HCl (Figure 13), which we use as a proxy for chlorine activation. The
698 initial HCl values in early June were lower in 2019 than in 2018 by up to 0.4 ppbv. The negative
699 differences seen in Figure 13c between 600 K and 750 K indicate stronger chlorine activation in
700 2019 and are consistent with larger areas below T_{NAT} in that layer (see Figure 12c). This is
701 particularly evident at the end of August and in early September when the low temperatures
702 extended higher in 2019 than in the preceding year. Positive 2019-2018 HCl differences of up to
703 0.7 ppbv in the 400 K – 550 K layer in late August provide evidence that chlorine deactivation
704 occurred about two weeks earlier in 2019 than it did in 2018, again, consistent with the T_{NAT}
705 results.
706
707 We estimate the chemical contribution to the polar vortex ozone change using a variation of the
708 passive tracer subtraction method introduced by Manney et al. (1995a, b). We use the additional
709 assimilation experiments with an idealized passive tracer initialized with the assimilated ozone on
710 30 May. As this passive "ozone" is subject to transport only, the chemical contribution to ozone

changes can be calculated by differencing it with the assimilated ozone. This approach comes with two caveats. First, constituent assimilation corrects for inaccuracies in both the model chemistry and transport, and there is no clear way to separate the two. Therefore, some of the differences between the passive tracer and ozone result not from chemistry but from transport errors. We will return to this point in Section 5. Second, the difference between the assimilated ozone and the passive tracer shown below should not be interpreted simply as a result of local ozone depletion. Instead, they represent the cumulative effect of potentially complex chemistry (not only chemical ozone loss in the lower stratosphere, but also chemical production in the middle and upper stratosphere) along air parcel trajectories between 30 May and any given date. As such, these differences are not independent of transport.

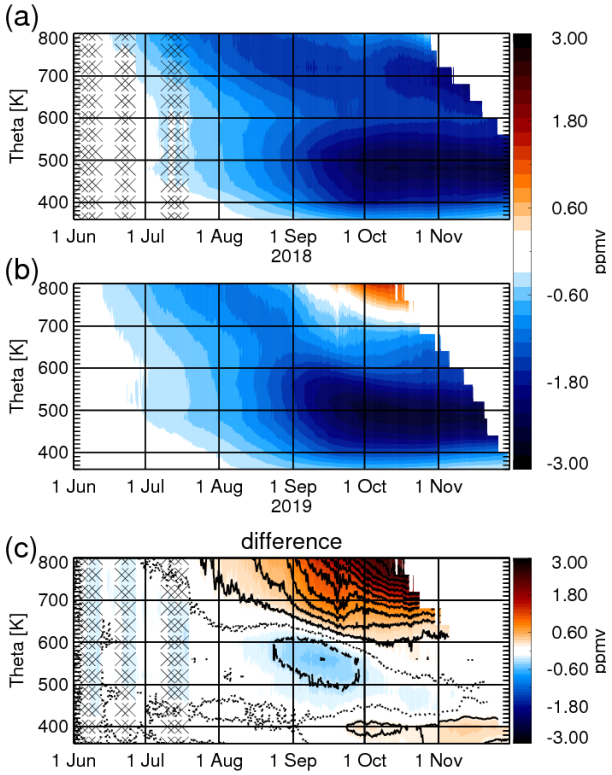

Figure 14. *Difference between assimilated ozone and the passive tracer mixing ratio as functions of time and potential temperature in 2018 (a) and 2019 (b), and the difference between the two (c). The contour spacing in (c) is 0.25 ppmv. The periods in 2018 for which MLS data do not exist are indicated by hatching.*

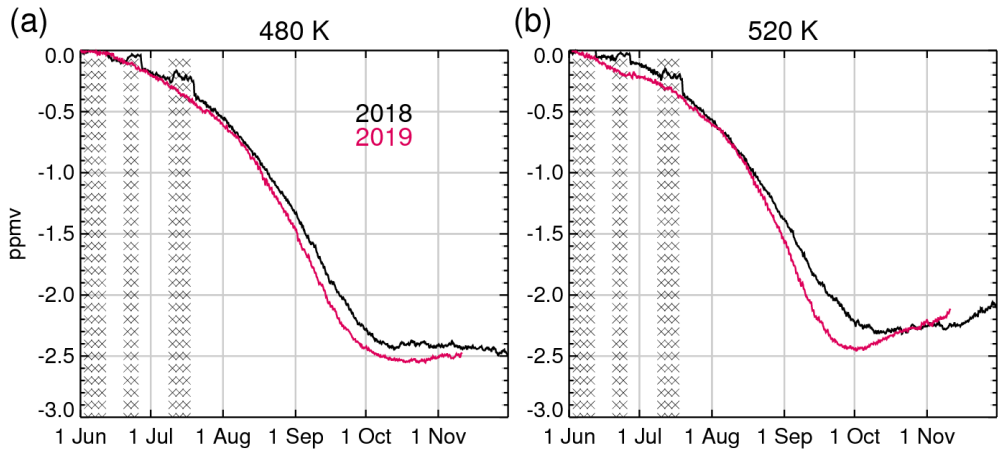

Figure 15. *Difference between assimilated ozone and the passive tracer mixing ratio at 480 K (a) and 520 K (b) as functions of time for 2018 (black) and 2019 (red). The periods in 2018 for which MLS data do not exist are indicated by hatching.*

The results of passive tracer subtraction are shown in Figures 14, 15, and 16 for 2018 and 2019. Figure 14 shows the vortex averaged differences between the assimilated ozone and the passive tracer as functions of potential temperature and time. It also plots the difference between the two years. In both, 2018 and 2019 there were descending layers of negative differences resulting from gas-phase chemistry between 600 K and 800 K from July and September. Non-negligible ozone depletion in that layer is in agreement with the findings of Livesey et al. (2015) (their Figure 6), however it does not significantly contribute to vortex-integrated loss, as shown in our discussion of Figure 16 below. The impact of heterogeneous chemistry on the ozone mixing ratios was largest between 400 K and 600 K starting in August, consistent with catalytic destruction of ozone by chlorine activated on the surfaces of PSCs. The maximum loss occurred at about 500 K starting mid-September in both years. Figure 15, which shows the impacts of chemistry at 480 K and 520 K, reveals that the intensity of ozone depletion was slightly greater in 2019 than in 2018, reaching 2.5 ppm at both levels at the end of September. These results are quantitatively similar to the chemical ozone depletion estimates obtained by Livesey et al. (2015) using a match-based method (their Figure 6). However, we note that that technique produced estimates based on 15-day trajectories, in contrast to our approach that implicitly folds in the entire "chemical history" of air parcels, as explained above. Figure 14c clearly shows the impact of the different dynamical conditions between the two years on the vortex chemistry above 600 K. As seen in Figure 10 the mid-stratospheric portion of the vortex was strongly displaced towards the midlatitudes, and, consequently, more exposed to sunlight (Movie S3). In addition, in 2019 there was a strong diabatic descent in that layer associated with the SSW that lasted through October and transported photochemically ozone-enriched air from the upper stratosphere (Figure S1). To summarize the results shown in Figures 14 and 15, the overall impact of chemistry on the 2018–2019 vortex-averaged ozone differences was large above 600 K but fairly small in the lower portion of the vortex, where the effects of early chlorine deactivation were not seen until late September, and even then only around 400 K.

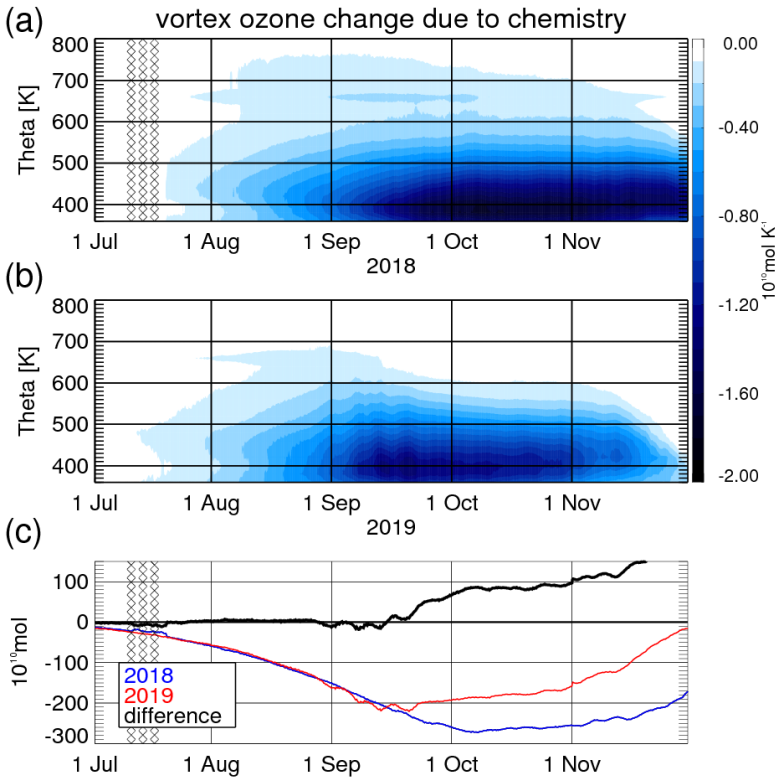

Figure 16. *Time series of the change in the polar vortex ozone content in moles due to chemical processes, calculated using the passive tracer subtraction method. The top two panels show the ozone change in moles per degree Kelvin between 360 K and 800 K for 2018 (a) and 2019 (b). The total vortex ozone change computed by integrating over the layers is shown in panel (c) for 2018 (blue) and 2019 (red). The black line is the difference between the two. The periods in 2018 for which MLS data do not exist are indicated by hatching.*

Next, we examine the assimilated ozone – passive tracer differences expressed in moles of ozone per 1-K isentropic layer (Figure 16). This method of presentation combines the ozone changes due to chemistry and the effects of the changing polar vortex area at each layer and, unlike the average mixing ratio, provides a measure of the ozone content changes integrated over the entire lower and middle-stratospheric polar vortex. Unlike the previous figures in this study, Figure 16 covers the period from July to November as the impacts of chemistry were small in June. In both years, the largest changes occurred in the lowest portion of the vortex because of a relatively high air density there. There was a gradual decrease in the ozone content between August and mid-September in both 2018 and 2019. In 2018, that tendency continued until the end of September, and the ozone/passive tracer differences remained approximately constant for about a month thereafter. In contrast, in 2019 the differences started increasing (becoming less negative) in the second half of September and continued to increase slowly throughout October. A comparison with Figures 9 and 13 suggests that this increase was due to the shrinking size of the polar vortex followed by early termination of chemical depletion. Figure 16c shows the ozone–passive tracer difference summed between 360 K and 800 K. The evolution of the vortex ozone content was almost identical between the two winters until mid-September, resulting in a total ozone loss of 200×10^{10} moles. By early October the loss reached approximately 270×10^{10} moles in 2018 but the 2019 ozone had begun to recover. At the end of November, the 2019 ozone-passive tracer difference was back to

nearly zero while in 2018 it was 180×10^{10} moles or 66% of the maximum loss. The combined effects of differences in chemical loss, diabatic descent, and the vortex size led to the vortex ozone content decrease at the end of October 2019 at 60% of that in 2018. These numbers do not translate directly into the size of the ozone hole (Figure 1), which in 2019 was 60% of that in 2018 already at the beginning of September and 25% of that in 2018 by the end of October. These results indicate a dominant role of the three-dimensional vortex geometry in the anomalously low total ozone column and the ozone hole size in 2019, as elaborated in our discussion of Figure 10.

5. Uncertainties related to transport

The ozone loss estimates presented in the previous section come with uncertainties primarily related to model transport errors in the passive ozone tracer. Transport errors arise from inaccuracies in both diabatic motions within the polar vortex and mixing across the vortex edge. Consequently, they are difficult to estimate using the available suite of tracers and data. In this section, we only attempt a somewhat crude estimate of transport errors resulting from vortex-averaged diabatic processes within the vortex. As suggested by Figures 4 and 5, mixing, while present, plays a relatively small role below the 600 K potential temperature level where most ozone depletion occurs. We calculate approximate vortex-averaged rates of descent from assimilated N_2O and a separate experiment, in which N_2O was "passive" (not assimilated) and apply the differences between the two (representing estimates of vertical motion errors) to the vortex-averaged passive ozone tracer gradients.

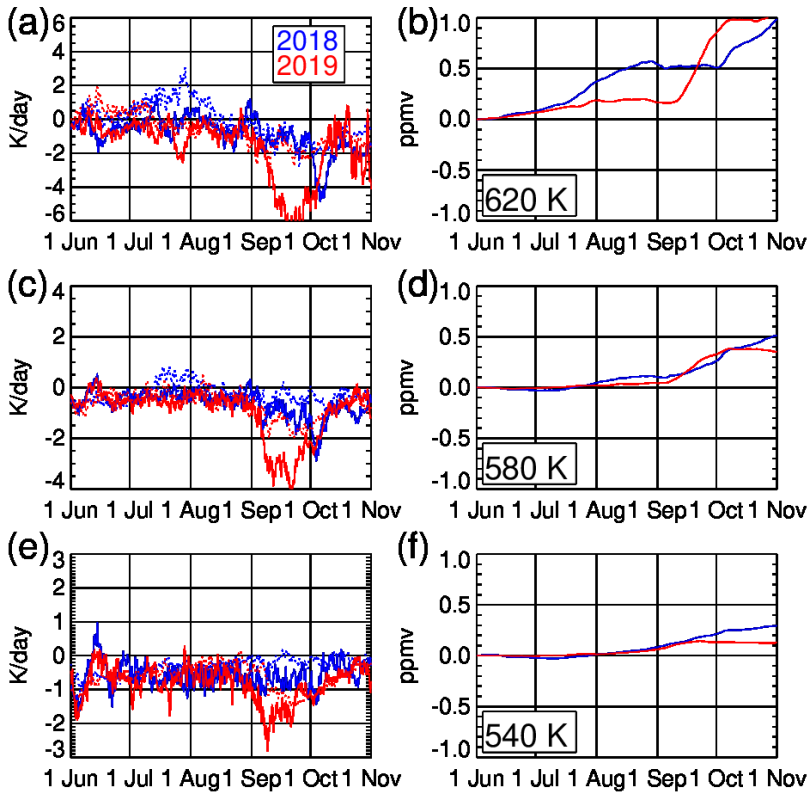

Figure 17. *Left column: approximate vortex-averaged rate of diabatic motion estimated from assimilated (solid) and passive (dotted) N_2O in 2018 (blue) and 2019 (red) at 620 K (a), 580 K (c), and 540 K (e). Negative values correspond to descent. Right column: The differences in diabatic motion rates between passive and active N_2O multiplied by passive ozone vertical gradients integrated in time between 1 June and a given time in 2018 and 2019 at 620 K (b), 580 K (d), and 540 K (f). These values estimate the passive ozone tracer errors resulting from transport. Positive numbers indicate that the passive tracer mixing ratio is likely underestimated.*

We show the results in Figure 17. We note several caveats. First, the notion of vortex-averaged diabatic descent rate, while used in previous ozone loss estimates (Manney et al., 2006; Jin et al., 2006; WMO 2007) is an approximate one as it relies on the assumption that the actual descent rate varies little across the vortex area at any given isentropic level (Ray et al., 2002; Plumb et al., 2007) and that mixing across the vortex edge is negligible (Livesey et al. 2015). Because of differential vertical motion as well as mixing, mean diabatic rates calculated from different tracers will in general be different. Second, by applying the estimated errors in diabatic rates to the passive ozone tracer gradients we implicitly assume that these gradients and their evolution are correct. Third, the vertical range within which N_2O is useful for these calculations is limited, as explained in the discussion of Figure 7. Because of these factors our confidence in these calculations is limited and we present them mainly as a first step toward uncertainty analysis for future chemical ozone loss estimates. Panels a, c, and e of Figure 17 show vortex-averaged diabatic transport rates, defined as the rate of change of potential temperature, calculated from passive and assimilated N_2O. The rates were mainly negative indicating diabatic descent, reaching up to about 2 K per day before the 2019 SSW. Following the onset of the SSW, there was a rapid acceleration of the descent, with the

rates reaching −6 K per day at the 620 K level. That acceleration was significantly underestimated by the model transport driven by assimilated winds, as seen in the red dotted lines representing passive N_2O. This underestimate is consistent with the behavior of the residual circulation in a GEOS model simulation of the 2009 Arctic SSW (Wargan and Coy, 2016). The right-hand side panels of Figure 17 show the estimated cumulative errors in the passive ozone tracer mixing ratios in 2018 and 2019. Positive values indicate insufficient diabatic descent and translate into underestimates of chemical ozone depletion in Figures 14, 15, and 16. The errors are largest at 620 K (up to 1 ppmv or 80% more ozone depletion) and smallest at 540 K (no greater than 0.3 ppmv or 15% more depletion). We note however, that the magnitude of ozone depletion in terms of the molar content (Figure 16) at 520 K is at most 25% of that at the peak level,400 K. At 620 K the number is only 10%. Assuming that the magnitude of the error continues to decrease with decreasing potential temperature, the resulting underestimate of ozone depletion is relatively small. Furthermore, the relative magnitude and sign of the errors in 2019 and 2018 suggest that the depletion is underestimated slightly more in 2019 than in 2018, strengthening our conclusion that the vortex averages of chemically depleted ozone in 2019 and 2018 were similar in both years, and the main impacts of the SSW on ozone came from the vortex geometry and volume.

6. Conclusions

We have used a novel configuration of the GEOS data assimilation system with a chemistry model to analyze the anomalous evolution of the Antarctic polar vortex ozone associated with the minor SSW that occurred in late August – early September 2019 and compare it with the more typical case of 2018. Assimilation of ozone, HCl and N_2O data from the MLS instrument into GEOS driven by meteorological analyses from the MERRA-2 reanalysis allowed a comprehensive study of the dynamical and chemical factors that directly influenced the 2019 Antarctic ozone. This work is the first one to explore the utility of the recently developed stratospheric chemical data assimilation capability in GEOS for scientific inquiry. It is a part of an ongoing effort to produce a mission-long reanalysis of MLS constituent observation.

We summarize our main findings as follows.

- The area of the 2019 ozone hole started diverging from the MERRA-2 climatology and the 2018 case at the beginning of September. The area stayed between $5{\cdot}10^6$ km^2 and $10{\cdot}10^6$ km^2 in September and October 2019, compared to $20{\cdot}10^6$ km^2 and $25{\cdot}10^6$ km^2 in 2018.
- The combined effects of chemistry and diabatic descent (stronger in 2019) contributed to very similar magnitude of ozone depletion in the 360 K – 600 K layer in both years; in fact, somewhat stronger depletion (between 0.25 ppmv and 0.5 ppmv) occurred in 2019 between 500 K and 600 K in September.
- Vortex size (smaller in 2019) had a larger effect than chemistry did. Chemical depletion together with the differences in the size of the 2019 and 2018 vortices, the cumulative end of October vortex ozone loss in 2019 was 60% of that in 2018 (Figure 16c).
- The anomalous geometry of the polar vortex (its tilt and decrease in size with altitude) accounted for all of the difference in the ozone hole area between 2018 and 2019 during the first half of September and more than half of the difference afterward.

The fact that the vortex-averaged LS chemical ozone depletion in 2019 was not significantly different than that in 2018 until mid-September resembles the findings of Sinnhuber et al. (2003),

who estimated chemical depletion south of 60°S for the major SSW year 2002 and found it to not be significantly different than that in the more typical years 2000 and 2001, and attributed all of the difference between the polar ozone in 2002 and other years to dynamics. Weber et al. (2003) reached similar conclusions based on an analysis of observed OClO column amounts. Hoppel et al. (2003) estimated the 2002 chemical ozone loss within the vortex to be about 20% lower than in typical years *after* the SSW occurred. These findings are compatible with ours for the 2019 austral summer/spring season. Similarly, the dominant role of the overlaying of the ozone-rich upper-stratospheric air in the anomalously small ozone hole area was previously identified for the 2002 case by Allen et al. (2003), Kondragunta et al., 2005, Randall et al. (2005), and Yela et al. (2005). These findings were summarized in WMO (2007). These similarities may seem remarkable, given the 'minor' character of the 2019 SSW, compared to the major SSW of 2002. However, we reiterate that the 2019 event was significant. A NH vortex disturbance as far outside the climatological envelope as the 2019 SH event would entail a 10 hPa 60°N average wind reversal, and it would fall under the category of a major SSW. Echoing a study of the 2014/2015 Arctic polar winter by Manney et al. (2015), the 2019 event can be regarded as *a minor sudden stratospheric warming with a major impact*.

Acknowledgments

Funding for this research was provided by NASA's Modeling, Analysis and Prediction grant "A new look at stratospheric chemistry with multispecies chemical data assimilation". Work at the Jet Propulsion Laboratory, California Institute of Technology, was done under contract with NASA. Resources supporting this work were provided by the NASA High-End Computing (HEC) Program through the NASA Center for Climate Simulation at Goddard Space Flight Center (GSFC). MERRA-2 is an official product of the Global Modeling and Assimilation Office at NASA GSFC, also supported by MAP. ACE-FTS is the primary instrument on the SCISAT satellite, a Canadian-led mission mainly supported by the Canadian Space Agency. ACE-FTS data were downloaded from http://www.ace.uwaterloo.ca/data.php. The South Pole ozonesonde data are curated by the National Oceanic and Atmospheric Administration's Earth System Laboratory and can be downloaded from https://esrl.noaa.gov/gmd/dv/data/. The MERRA-2 data are available in these in-text data citation references: GMAO 2015a,b,c. Assimilation output used in this study resides in the NASA public repository https://gmao.gsfc.nasa.gov/gmaoftp/STRATOSPHERE/ozone-hole-2019/
.

References

Allen, D. R., Bevilacqua, R. M., Nedoluha, G. E., Randall, C. E., and Manney, G. L. (2003). Unusual stratospheric transport and mixing during the 2002 Antarctic winter, *Geophys. Res. Lett.*, 30, 1599, https://doi.org/10.1029/2003GL017117, 12.

Baldwin, M. P., Hirooka, T., O'Neill, A., and Yoden, S. (2003). Major stratospheric warming in the Southern Hemisphere in 2002: Dynamical aspects of the ozone hole split. *SPARC Newsletter,* 20, SPARC Office, Toronto, ON, Canada,24–26.

Ball, W. T., Alsing, J., Mortlock, D. J., Rozanov, E. V., Tummon, F., and Haigh, J. D. (2017), Reconciling differences in stratospheric ozone composites. *Atmos. Chem. Phys., 17, 12269-12302*, doi:10.5194/acp-17-12269-2017.

Ball, W. T., Alsing, J., Mortlock, D. J., Staehelin, J., Haigh, J. D., Peter, T. et al. (2018). Evidence for a continuous decline in lower stratospheric ozone offsetting ozone layer recovery, *Atmos. Chem. Phys*., 18, 1379-1394, https://doi.org/10.5194/acp-18-1379-2018

Bell, G.D., Halpert, M.S., Ropelewski, C.F., Kousky, V.E. , Douglas, A.V. , Schnell, R.C. and Gelman, M.E. (1999). Climate Assessment for 1998. *Bull. Amer. Meteor. Soc.,* **80**, S1–S48, https://doi.org/10.1175/1520-0477-80.5s.S1

Bernath, P. F., McElroy, C. T., Abrams, M. C., Boone, C. D., Butler, M., Camy-Peyret, et al. (2005). Atmospheric Chemistry Experiment (ACE): Mission overview, *Geophys. Res. Lett*., 32, L15S01, https://doi.org/10.1029/2005GL022386

Bernath, P.F. (2017). The Atmospheric Chemistry Experiment (ACE), *Journal of Quantitative Spectroscopy and Radiative Transfer,* Volume 186, 2017, Pages 3 16, ISSN 0022-4073, https://doi.org/10.1016/j.jqsrt.2016.04.006

Bourassa, A. E., Degenstein, D. A., Randel, W. J., Zawodny, J. M., Kyrölä, E., McLinden, C. A., Sioris, C. E., and Roth, C. Z. (2014), Trends in stratospheric ozone derived from merged SAGE II and Odin-OSIRIS satellite observations, *Atmos. Chem. Phys., 14, 6983-6994*, doi:10.5194/acp-14-6983-2014.

Brasseur, G. P.*, and* S. Solomon (2005): Aeronomy of the Middle Atmosphere*,* 3rd ed.*, Springer,* New York.

Butchart, N. and E.E. Remsberg (1986). The area of the stratospheric polar vortex as a diagnostic for tracer transport on an isentropic surface, *J. Atmos. Sci*., 43, 1319–1339.

969 Butler, A. H., Sjoberg, J. P., Seidel, D. J., and Rosenlof, K. H. (2017). A sudden stratospheric
970 warming compendium, *Earth Syst. Sci. Data*, 9, 63–76, https://doi.org/10.5194/essd-9-63-
971 2017
972
973 Cohn, S. E. (1997). An introduction to estimation theory. *J. Meteor. Soc. Japan*, 75, 257–288.
974
975 Desrosiers, G., Berre, L., Chapnik, B., and Poli, P. (2005). Diagnosis of observation, background
976 and analysis error statistics in observation space, *Q. J. Roy. Meteor. Soc.*, 131, 3385–3396,
977 https://doi.org/10.1256/qj.05.108
978
979 Douglass, A. R., Rood, R. B., Kawa, S. R., & Allen, D. J. (1997),. A 3D simulation of the
980 evolution of the middle latitude winter ozone in the middle stratosphere, *J. Geophys. Res.,*
981 102(D15), 19,217–19,232, https://doi.org/10.1029/97JD01043
982
983 Dunkerton, T. J., & Delisi, D. P. (1986). Evolution of potential vorticity in the winter
984 stratosphere of January-February 1979. Journal of Geophysical Research, 91, 1199–1208.
985
986 Eldering, A., Wennberg, P. O., Crisp, D., Schimel, D. S., Gunson, M. R., Chatterjee, A. et al.
987 (2017). The Orbiting Carbon Observatory-2 early science investigations of regional carbon
988 dioxide fluxes, *Science*, 358, 305eaam5745, doi: 10.1126/science.aam5745
989
990 Errera, Q., Chabrillat, S., Christophe, Y., Debosscher, J., Hubert, D., Lahoz, W., Santee, M. L.,
991 Shiotani, M., Skachko, S., von Clarmann, T., and Walker, K. (2019). Technical note:
992 Reanalysis of Aura MLS chemical observations, *Atmos. Chem. Phys.,* 19, 13647–13679,
993 https://doi.org/10.5194/acp-19-13647-2019, 2019
994
995 Farman, J.C., Gardiner, B.G. and Shanklin, J.D. (1985). J. Large losses of total ozone in
996 Antarctica reveal seasonal ClO_x/NO_x interaction. *Nature* 315**,** 207–210.
997 https://doi.org/10.1038/315207a0
998
999 Froidevaux, L.*,* et al. (2008a). Validation of Aura Microwave Limb Sounder stratospheric ozone
1000 measurements*, J. Geophys. Res*.*,* 113*(*D15*),* D15S20*,* https://doi.org/10.1029/2007JD008771
1001
1002 Froidevaux, L., et al. (2008b). Validation of Aura Microwave Limb Sounder HCl measurements,
1003 *J. Geophys. Res*.,113 (D15), D15S25, https://doi.org/10.1029/2007JD009025
1004
1005 Gelaro, R., McCarty, W., Suárez, M.J., Todling, R., Molod, A., Takacs, L. et al., (2017). The
1006 Modern-Era Retrospective Analysis for Research and Applications, Version 2 (MERRA-2).
1007 *J. Climate, 30, 5419–5454,* https://doi.org/10.1175/JCLI-D-16-0758.1
1008
1009 Global Modeling and Assimilation Office (GMAO) (2015a), MERRA-2 inst3_3d_asm_Np:
1010 3d,3-Hourly,Instantaneous,Pressure-Level,Assimilation,Assimilated Meteorological Fields
1011 V5.12.4, Greenbelt, MD, USA, Goddard Earth Sciences Data and Information Services
1012 Center (GES DISC), Accessed: January 2020, 10.5067/QBZ6MG944HW0
1013

Global Modeling and Assimilation Office (GMAO) (2015b), MERRA-2 inst1_2d_asm_Nx: 2d,1-Hourly,Instantaneous,Single-Level,Assimilation,Single-Level Diagnostics V5.12.4, Greenbelt, MD, USA, Goddard Earth Sciences Data and Information Services Center (GES DISC), Accessed: January 2020, 10.5067/3Z173KIE2TPD

Global Modeling and Assimilation Office (GMAO) (2015c), MERRA-2 tavg3_3d_asm_Nv: 3d,3-Hourly,Time-Averaged,Model-Level,Assimilation,Assimilated Meteorological Fields V5.12.4, Greenbelt, MD, USA, Goddard Earth Sciences Data and Information Services Center (GES DISC), Accessed: January 2020, 10.5067/SUOQESM06LPK

Harris, N. R. P., Hassler, B., Tummon, F., Bodeker, G. E., Hubert, D., Petropavlovskikh, I. et al (2015). Past changes in the vertical distribution of ozone – Part 3: Analysis and interpretation of trends, *Atmos. Chem. Phys., 15, 9965-9982*, doi:10.5194/acp-15-9965-2015.

Hassler, B., Daniel, J. S., Johnson, B. J., Solomon, S. & Oltmans, S. J. (2011). An assessment of changing ozone loss rates at South Pole: Twenty-five years of ozonesonde measurements. *J. Geophys. Res.* 116, D22301, doi:10.1029/2011JD016353

Hendon, H. H., D. W. Thompson, E.-P. Lim, et al. (2019). Rare forecasted climate event under way in the Southern Hemisphere. *Nature*, 573 (7775): 495-495 https://doi.org/10.1038/d41586-019-02858-0

Hood, L. L., Soukharev, B. E., Fromm, M., and McCormack, J. P (2001). Origin of extreme ozone minima at middle to high northern latitudes, J. Geophys. Res.-Atmos., 106, 20925–20940, https://doi.org/10.1029/2001JD900093

Hoppel, K., Bevilacqua, R. M., Allen, D. R., Nedoluha, G., and Randall, C. E. (2003). POAM III observations of the anomalous 2002 Antarctic ozone hole, *Geophys. Res. Lett.*, 30, 1394, https://doi.org/10.1029/2003GL016899

Iwao, K. and Hirooka, T. (2006). Dynamical quantifications of ozone mini-hole formation in both hemispheres, J. Geophys. Res.-Atmos., 111, d02104, https://doi.org/10.1029/2005JD006333

Jaeglé, L., Wood, R., & Wargan, K. (2017). Multiyear composite view of ozone enhancements and stratosphere-to-troposphere transport in dry intrusions of northern hemisphere extratropical cyclones. *Journal of Geophysical Research: Atmospheres*, 122, 13,436– 13,457. https://doi.org/10.1002/2017JD027656

Jin, J. J., et al. (2006), Severe Arctic ozone loss in the winter 2004/2005: observations from ACE-FTS, *Geophys. Res. Lett.*, 33, L15801, https://doi.org/10.1029/2006GL026752

Johnson, B. J., Cullis, P.D. and NOAA ESRL (2018). Earth System Research Laboratory Ozone Water Vapor Group Ozonesonde Measurements, Version 1. South Pole ozonesondes. NOAA National Centers for Environmental Information. doi:10.7289/V5CC0XZ1, accessed: November 2019

Kawa, S. R., Kumer, J. B., Douglass, A. R., Roche, A. E., Smith, S. E., Taylor, F. W., & Allen, D. J. (1995), Missing chemistry of reactive nitrogen in the upper stratospheric polar winter, *Geophys. Res. Lett*., 22, 2629–2632, https://doi.org/10.1029/95GL02336

Knowland, K. E., Ott, L. E., Duncan, B. N., & Wargan, K. (2017). Stratospheric intrusion-influenced ozone air quality exceedances investigated in the NASA MERRA-2 reanalysis. *Geophys. Res. Lett,* 44, 10,691–10,701. https://doi.org/10.1002/2017GL074532

Komhyr, W.D., Grass, R.D., and Leonard, R.K. (1986). Total ozone decrease at South Pole, Antarctica, 1964-1985. *Geophys. Res. Lett.*, 13, 1248–1251. https://doi.org/10.1029/GL013i012p01248

Kondragunta, S., Flynn, L.E., Neuendorffer, A., Miller, A.J., Long, C., Nagatani, R., Zhou, S., Beck, T., Beach, E., McPeters, R., Stolarski, R., Bhartia,P.K., DeLand, M.T. and Huang, L (2005). Vertical Structure of the Anomalous 2002 Antarctic Ozone Hole. *J. Atmos. Sci.,* **62**, 801–811, https://doi.org/10.1175/JAS-3324.1

Lambert, A., et al. (2007). Validation of the Aura Microwave Limb Sounder stratospheric water vapor and nitrous oxide measurements, *J. Geophys. Res*., 112 (D24), D24S36, https://doi.org/10.1029/2007JD008724

Lawrence, Z. D., Manney, G. L., and Wargan, K. (2018). Reanalysis intercomparisons of stratospheric polar processing diagnostics, *Atmos. Chem. Phys*., 18, 13547–13579, https://doi.org/10.5194/acp-18-13547-2018

Levelt, P. F., van den Oord, G. H. J., Dobber, M. R., Mälkki, A., Visser, H., Vries, J. D., Stammes, P., Lundell, J. O. V., & Saari, H. (2006). The Ozone Monitoring Instrument, *IEEE Trans. Geosci. Remote Sens*., 44, 1093–1101, https://doi.org/10.1109/TGRS.2006.872333

Levelt, P. F., Joiner, J., Tamminen, J., Veefkind, J. P., Bhartia, P. K., Stein Zweers, D. C., Duncan, B., et al. (2018). The Ozone Monitoring Instrument: overview of 14 years in space, *Atmos. Chem. Phys*., 18, 5699-5745, https://doi.org/10.5194/acp-18-5699-2018

Livesey, N. J., Santee, M. L., and Manney, G. L. (2015). A Match-based approach to the estimation of polar stratospheric ozone loss using Aura Microwave Limb Sounder observations, *Atmos. Chem. Phys.*, 15, 9945–9963, https://doi.org/10.5194/acp-15-9945-2015, 2015.

Livesey, N.J., Read, W.G., Wagner, P.A., Froidevaux, L., Lambert, A., Manney, G.L., et al. (2018). Version 4.2x Level 2 data quality and description document. *JPL D-33509 Rev. D*, available from https://mls.jpl.nasa.gov/data/v4-2_data_quality_document.pdf

Mahieu, E., Duchatelet, P., Demoulin, P., Walker, K. A., Dupuy, E., Froidevaux, L. et al. (2008). Validation of ACE-FTS v2.2 measurements of HCl, HF, CCl_3F and CCl_2F_2 using space-,

balloon- and ground-based instrument observations, *Atmos. Chem. Phys*., 8, 6199–6221, https://doi.org/10.5194/acp-8-6199-2008

Manney, G.L., Zurek, R.W., O'Neill, A. and Swinbank, R. (1994). On the motion of air through the stratospheric polar vortex, *J. Atmos. Sci.*, 51, 2973-2994.

Manney, G. L., Zurek, R. W., Froidevaux, L., Waters, J. W., O'Neill, A., and Swinbank, R. (1995a). Lagrangian transport calculations using UARS Data, Part II: Ozone, *J. Atmos. Sci.,* 52, 3069–3081.

Manney, G. L., Zurek, R. W., Lahoz, W. A., Harwood, R. S., Gille, J. C., Kumer, J. B. et al. (1995b). Lagrangian transport calculations using UARS Data, Part I: Passive tracers, *J. Atmos. Sci*., 52, 3049–3068.

Manney, G.L., Sabutis, J.L., Allen, D.R., Lahoz, W.A., Scaife, A.A.C.E. Randall, A.A. et al. (2005). Simulations of Dynamics and Transport during the September 2002 Antarctic Major Warming. *J. Atmos. Sci.,* **62**, 690–707, https://doi.org/10.1175/JAS-3313.1

Manney, G. L., Santee, M. L., Froidevaux, L., Hoppel, K., Livesey, N. J., and Waters, J. W. (2006), EOS MLS observations of ozone loss in the 2004–2005 Arctic winter, *Geophys. Res. Lett.*, 33, L04802, https://doi.org/10.1029/2005GL024494

Manney, G. L., Lawrence, Z. D., Santee, M. L., Read, W. G., Livesey, N. J., Lambert, A., Froidevaux, L., Pumphrey, H. C., and Schwartz, M. J. (2015), A minor sudden stratospheric warming with a major impact: Transport and polar processing in the 2014/2015 Arctic winter, *Geophys. Res. Lett.*, 42, 7808– 7816, https://doi.org/10.1002/2015GL065864

Naujokat, B. and Roscoe, H.K. (2005). Evidence against an Antarctic Stratospheric Vortex Split during the Periods of Pre-IGY Temperature Measurements. *J. Atmos. Sci.,* **62**, 885–889, https://doi.org/10.1175/JAS-3317.1

Nash, E. R., P. A. Newman, J. E. Rosenfield, and M. R. Schoeberl (1996), An objective determination of the polar vortex using Ertel's potential vorticity, J. Geophys. Res., 101(D5), 9471–9478, https://doi.org/10.1029/96JD00066.

Newman, P. A., Lait, L. R., and Schoeberl, M. R. (1988). The morphology and meteorology of southern hemisphere spring total ozone mini-holes, *Geophys. Res. Lett*., 15, 923–926, https://doi.org/10.1029/GL015i008p00923.

Newman, P. A. and Nash, E. R. (2005). The unusual Southern Hemisphere stratosphere winter of 2002. *J. Atmos. Sci*.,62, 614–628, https://doi.org/10.1175/JAS-3323.1

Nielsen, J. E., Pawson, S., Molod, A., Auer, B., da Silva, A. M., Douglass, A. R., et al. (2017). Chemical mechanisms and their applications in the Goddard Earth Observing System (GEOS) earth system model. *J. Adv. Mod. Earth Sys.,* 9, 3019– 3044. https://doi.org/10.1002/2017MS001011

Orbe, C., Oman, L. D., Strahan, S. E., Waugh, D. W., Pawson, S., Takacs, L. L., & Molod, A. M. (2017). Large-scale atmospheric transport in GEOS replay simulations. *J. Adv. Mod. Earth Sys.*, 9. https://doi. org/10.1002/2017MS001053

Orbe, C., Wargan, K., Pawson, S., & Oman, L. D. (2020). Mechanisms linked to recent ozone decreases in the Northern Hemisphere lower stratosphere. *Journal of Geophysical Research: Atmospheres*, 125, e2019JD031631. https://doi.org/10.1029/2019JD031631

Plumb, R. A. (2007). Tracer interrelationships in the stratosphere, *Rev. Geophys.*, 45, RG4005, https://doi. org/10.1029/2005RG000179

Purser, R. J., Wu, W.-S.,Parrish, D. F. and Roberts, N. M. (2003a). Numerical aspects of the application of recursive filters to variational statistical analysis. Part I: spatially homogeneous and isotropic Gaussian covariances, *Mon. Wea. Rev.*, 131, 1524-1535.

Purser, R. J., Wu, W.-S., Parrish, D. F. and Roberts, N. M. (2003b). Numerical aspects of the application of recursive filters to variational statistical analysis. Part II: spatially inhomogeneous and anisotropic general covariances, *Mon. Wea. Rev.,* 131, pp. 1536-1548.

Randall, C.E., Manney, G.L., Allen, D.R., Bevilacqua, R.M., Hornstein, J., Trepte, C. et al. (2005). Reconstruction and Simulation of Stratospheric Ozone Distributions during the 2002 Austral Winter. *J. Atmos. Sci.,* **62**, 748–764, https://doi.org/10.1175/JAS-3336.1

Ray, E. A., Moore, F. L., Elkins, J. W., Hurst, D. F., Romashkin, P. A., Dutton, G. S., and Fahey, D. W. (2002). Descent and mixing in the 1999–2000 northern polar vortex inferred from in situ tracer measurements, *J. Geophys. Res.*, 107(D20), 8285, https://doi.org/10.1029/2001JD000961

Roscoe, H.K.; Shanklin, J.D.; Colwell, S.R. (2005). Has the Antarctic Vortex Split before 2002? *Journal of the Atmospheric Sciences*, 62 (3). 581-588. https://doi.org/10.1175/JAS-3331.1

Santee, M.L. et al., (2007), Validation of the Aura Microwave Limb Sounder HNO3 measurements, *J. Geophys. Res.*, 112, D24S40, https://doi.org/10.1029/2007JD008721.

Santee, M. L., MacKenzie, I. A., Manney, G. L., Chipperfield, M. P., Bernath, P. F., Walker, K. A., et al. (2008). A study of stratospheric chlorine partitioning based on new satellite measurements and modeling, *J. Geophys. Res.*, 113, D12307, https://doi.org/10.1029/2007JD009057.

Scaife, A.A., Jackson, D.R., Swinbank, R., Butchart, N., Thornton, H.E., Keil, M. and Henderson, L. (2005). Stratospheric Vacillations and the Major Warming over Antarctica in 2002. *J. Atmos. Sci.,* **62**, 629–639, https://doi.org/10.1175/JAS-3334.1

Sheese, P. E., Walker, K. A., Boone, C. D., Bernath, P. F., Froidevaux, L., Funke, B., Raspollini, P. and von Clarmann, T. (2017). ACE-FTS ozone, water vapour, nitrous oxide, nitric acid,

and carbon monoxide profile intercomparisons with MIPAS and MLS, *J. Quant. Spectrosc. Radiat. Transf.,* https://doi.org/10.1016/j.jqsrt.2016.06.026

Sinnhuber, B.-M., Weber, M., Amankwah, A. and Burrows, J. P. (2003). Total ozone during the unusual Antarctic winter of 2002, *Geophys. Res. Lett*., 30(11), 1580, https://doi.org/10.1029/2002GL016798

Sofieva, V. F., Kyrölä, E., Laine, M., Tamminen, J., Degenstein, D., Bourassa, A. et al. (2017). Merged SAGE II, Ozone_cci and OMPS ozone profile dataset and evaluation of ozone trends in the stratosphere, *Atmos. Chem. Phys., 17, 12533-12552*, doi:10.5194/acp-17-12533-2017.

Solomon, S., Ivy, D. J., Kinnison, D., Mills, M. J., Neely, R. R., and Schmidt, A. (2016). Emergence of healing in the Antarctic ozone layer. *Science*, 353, 269–274, https://doi.org/10.1126/science.aae0061

SPARC/IO3C/GAW (2019). SPARC/IO3C/GAW Report on Long-term Ozone Trends 299 and Uncertainties in the Stratosphere, I. Petropavlovskikh, S. Godin-Beekmann, D. Hubert, R. 300 Damadeo, B. Hassler, V. Sofieva (Eds.), SPARC Report No. 9, GAW Report No. 241, WCRP301 17/2018, doi: 10.17874/f899e57a20b; www.sparc-climate.org/publications/sparc-reports.

Steinbrecht, W., Froidevaux, L., Fuller, R., Wang, R., Anderson, J., Roth et al. (2017). An update on ozone profile trends for the period 2000 to 2016, *Atmos. Chem. Phys., 17, 10675-10690*, https://doi.org/10.5194/acp-17-10675-2017

Stolarski, R., Krueger, A., Schoeberl, M., McPeters, R.D., Newman, P.A. and Alpert, J.C. (1986). Nimbus 7 satellite measurements of the springtime Antarctic ozone decrease. *Nature* **322,** 808–811, https://doi.org/10.1038/322808a0

Stolarski, R.S., R.D. McPeters, and P.A. Newman, 2005: The Ozone Hole of 2002 as Measured by TOMS. *J. Atmos. Sci.,* **62**, 716–720, https://doi.org/10.1175/JAS-3338.1

Strahan, S. E., Douglass, A. R., and Steenrod, S. D. (2016), Chemical and dynamical impacts of stratospheric sudden warmings on Arctic ozone variability, *J. Geophys. Res. Atmos.*, 121, 11,836– 11,851, https://doi.org/10.1002/2016JD025128.

Strahan, S. E., & Douglass, A. R. (2017). Decline in Antarctic ozone depletion and lower stratospheric chlorine deter- mined from Aura Microwave Limb Sounder observations. Geophysical Research Letters, 44, https://doi.org/10.1002/2017GL074830

Tangborn, A., Stajner, I., Buchwitz, M., Khlystova, I., Pawson, S., Burrows, J., Hudman, R., and Nedelec, P. (2009), Assimilation of SCIAMACHY total column CO observations: Global and regional analysis of data impact, *J. Geophys. Res.*, 114, D07307, https://doi.org/10.1029/2008JD010781.

Tangborn, A., Strow, L. L., Imbiriba, B., Ott, L., and Pawson, S.: Evaluation of a new middle-lower tropospheric CO_2 product using data assimilation, Atmos. Chem. Phys., 13, 4487–4500, https://doi.org/10.5194/acp-13-4487-2013, 2013.

Varotsos, C. (2002). The Southern Hemisphere ozone hole split in 2002. *Environ. Sci. Pollut. Res.*, 9,375–376. https://doi.org/10.1007/bf02987584

Wargan, K., Pawson, S., Olsen, M. A., Witte, J. C., Douglass, A. R., Ziemke, J. R., Strahan, S. E. and Nielsen, J. E. (2015), The global structure of upper troposphere-lower stratosphere ozone in GEOS-5: A multiyear assimilation of EOS Aura data. *J. Geophys. Res. Atmos.*, 120: 2013–2036. https://doi.org/10.1002/2014JD022493

Wargan, K. and Coy, L. (2016). Strengthening of the Tropopause Inversion Layer during the 2009 Sudden Stratospheric Warming: A MERRA-2 Study. *J. Atmos. Sci.,* **73**, 1871–1887, https://doi.org/10.1175/JAS-D-15-0333.1

Wargan, K., Labow, G., Frith, S., Pawson, S., Livesey, N., & Partyka, G. (2017). Evaluation of the Ozone Fields in NASA's MERRA-2 Reanalysis. *J. Climate*, 30, 2961–2988, https://doi.org/10.1175/JCLI-D-16-0699.1

Wargan, K., Orbe, C., Pawson, S., Ziemke, J. R., Oman, L. D., Olsen, M. A., et al. (2018). Recent decline in extratropical lower stratospheric ozone attributed to circulation changes. *Geophysical Research Letters*, 45, 5166– 5176. https://doi.org/10.1029/2018GL077406

Wargan, K., Kramarova, N., Weir, B., Pawson, S., & Davis, S. M. (2020). Toward a reanalysis of stratospheric ozone for trend studies: Assimilation of the Aura microwave limb sounder and ozone mapping and profiler suite limb profiler data. *Journal of Geophysical Research: Atmospheres*, 125, e2019JD031892. https://doi.org/10.1029/2019JD031892

Waters, J. W., Froidevaux, L., Harwood, R.S., Jarnot, R.F., Pickett, H.M., Read, W.G. et al. (2006). The Earth Observing System Microwave Limb Sounder (EOS MLS) on the Aura satellite. *IEEE Trans. Geosci. Remote Sens*., 44, 1075–1092. https://doi.org/10.1109/TGRS.2006.873771

Weber, M., Dhomse, S., Wittrock, F., Richter, A., Sinnhuber, B.-M., and Burrows, J. P. (2003). Dynamical control of NH and SH winter/spring total ozone from GOME observations in 1995–2002, *Geophys. Res. Lett.*, 30, 1583, https://doi.org/10.1029/2002GL016799

WMO (World Meteorological Organization) (2007). Scientific Assessment of Ozone Depletion: 2006. *Global Ozone Research and Monitoring Project* - Report No. 50, 572 pp., Geneva.

WMO (World Meteorological Organization) (2011) Scientific Assessment of Ozone Depletion: 2010, *Global Ozone Research and Monitoring Project*-Report No. 52, 516 pp., Geneva, Switzerland.

WMO (World Meteorological Organization) (2018). Scientific Assessment of Ozone Depletion: 2018. *Global Ozone Research and Monitoring Project*–Report No. 58, 588 pp., Geneva,

1286 Switzerland.

1287 Wu, W.-S., Purser, R. J. and Parrish, D. F. (2002). Three-dimensional variational analysis with
1288 spatially inhomogeneous covariances, *Mon. Wea. Rev.*, 130, 2905-2916.

1289 Yamazaki, Y., Matthias, V., Miyoshi, Y., Stolle, C., Siddiqui, T., Kervalishvili, G., et al. (2020),
1290 September 2019 Antarctic sudden stratospheric warming: Quasi-6-day wave burst and
1291 ionospheric effects. *Geophys. Res. Lett.Geophysical Research Letters*, 47, e2019GL086577.
1292 https://doi.org/10.1029/2019GL086577

1293 Yela, M., Parrondo, C., Gil, M., Rodríguez, S., Araujo, J., Ochoa, H., Deferrari, G. and Díaz, S.
1294 (2005). The September 2002 Antarctic vortex major warming as observed by visible
1295 spectroscopy and ozone soundings. *Int. J. Remote Sens*., 26:16,3361-3376,
1296 https://doi.org/10.1080/01431160500076285